HEAT TRANSFER ENHANCEMENT IN RECTANGULAR CHANNEL WITH COMPOUND COOLING TECHNIQUES

A Thesis

by

BELAL KRAD

Submitted to the Office of Graduate and Professional Studies of
Texas A&M University
in partial fulfillment of the requirements for the degree of

MASTER OF SCIENCE

Chair of Committee,	Je-Chin Han
Committee Members,	Robert Handler
	Hamn-Ching Chen
Head of Department,	Andreas Polycarpou

December 2013

Major Subject: Mechanical Engineering

ABSTRACT

Various compound internal cooling techniques were investigated in this experiment to see which combinations can offer the greatest heat transfer. Combinations of rib turbulators as well as pin-fins were used in different configurations in order to analyze heat transfer and pressure loss characteristics to determine which configuration had the overall best performance. Two different flow configurations were considered, a uniform channel flow setup as well as a jet impingement setup.

There were a total of sixteen cases performed for the experiment, eight for the channel flow and eight for the jet impingement. The types of cases that were performed were: a smooth surface case, two cases of only copper rib turbulators (P/e ratios of 5 and 10), two cases of only copper pin-fins (P/e ratios of 5 and 10), and three cases of a combinations of copper rib turbulators and pin-fins (P/e ratios of 2.5, 5, and 10). All of the cases were performed at four different Reynolds numbers to explore the effect of Reynolds number on the heat transfer.

In terms of the channel flow experiment, the results indicate that the all ribs case with a P/e ratio of 5 had the highest heat transfer coefficients but also produced the highest friction factor. If the total area is considered and not just the projected area, than the case of all pins P/e ratio of 10 is the best candidate due to its extensively low pressure drop and moderate heat transfer. In terms of the jet impingement experiment, none of the cases significantly enhanced heat transfer and many of them had results lower than the smooth case. The case of all pins P/e ratio of 5 performed the best out of

all the rough cases but the case of all pins P/e ratio of 10 perform the best when taking into account the total surface area. Cross-flow contributed to the jet impingement results, lowering the local Nusselt number due to the bending of the jet beams in the low x/d regions but started increasing the local Nusselt number at further x/d due to the cross flow heat transfer.

DEDICATION

I would like to first dedicate this thesis to my parents who have pushed me from a young age to pursue higher education and have given me constant emotional and financial support throughout my years. I would also like to dedicate it to the rest of my family and friends who have given me the emotional support that I needed in order to succeed.

ACKNOWLEDGEMENTS

First and foremost, I would like to thank God who has given me the opportunity to pursue this research and has blessed me throughout the way. He has given me the strength and patience that I needed throughout the challenges that I faced.

I would like to express my profound gratitude to my committee chair, Dr. Han, who has provided me with the support that I needed throughout the research process. I truly could not have benefited from the work if it was not for his excellent advising and mentoring. I would also like to thank my committee members, Dr. Chen, and Dr. Handler, for their assistance throughout the course of this research.

Finally, I would like to thank my colleagues who have provided me with assistance throughout this journey. So to Hao-Wei Wu, Hootan Zirakzadeh, Nafiz Khan Md., and Shang Yang, I truly appreciate all of the help and support that you gave me.

NOMENCLATURE

c_p	specific heat of gas (for air = 1005 J/KgK)
dj	diameter of the jet hole (m)
D_h	hydraulic diameter for channel flow arrangement (m)
e	rib height (m)
h	local heat transfer coefficient (W/m^2K)
k	thermal conductivity (for air at 25°C = 0.0257 W/mK)
$\dot{m}$	mass flow rate of air (kg/s)
w	mass flow rate (lbm/s)
$\dot{m}_j$	mass flow rate threw each jet hole (kg/s)
Nu	local Nusselt number based on hydraulic diameter
Nu_o	empirical Nusslet number
$\overline{Nu}$	Average Nusselt number
P	pitch between ribs
P_g	inlet gage pressure (psig)
P_s	local static pressure (in H_2O)
Pr	Prandtl Number (for air at 25°C = 0.713)
R	resistance (Ω)
q”	local heat flux (W/m^2)
q''_{loss}	local heat loss flux (W/m^2)
$\dot{Q}$	Total heat rate (W)
$\dot{Q}_{loss}$	Total heat loss rate (W)

Re	Reynolds number based on hydraulic diameter of channel flow setup
Rej	Reynolds number based on nozzle diameter for jet impingement
T_b	bulk temperature (°C)
T_e	exit temperature (°C)
T_i	inlet temperature (°C)
T_∞	room temperature (°C)
T_w	local surface temperature (°C)
V	voltage (V)
V	velocity of the air, (m/s)
A_c	cross-sectional area (m^2)
ν	kinematic viscosity of air (m^2/s)
ρ	density of air
D_1	Inner Pipe Diameter (in)
D_2	orifice diameter (in)
K	flow coefficient
p_1	inlet gage pressure (in Hg abs.)
S	a constant = 0.1145
Y	expansion factor
G	specific gravity of gas (for air, =1.00)
y	supercompressibility factor (for air, = 1.00)
Δp	pressure drop across orifice (in H_2O)
C_D	discharge coefficient
β	diameter ratio
κ	specific heat ratio

P	perimeter of channel flow cross-section (m)
A_p	projected area (m^2)
A_T	total area (m^2)
f	friction factor
f_0	empirical friction factor
dp/dx	pressure drop across channel (Pa/m)
TP	thermal performance
P_{Plenum}	pressure in the plenum
P_e	pressure inside of the jet channel
G_c	channel cross flow velocity based on channel cross-sectional area
G_j	jet mass velocity area based on jet diameter area
A_j	area based on jet hole diameter

TABLE OF CONTENTS

Page

Page

LIST OF FIGURES

Page

Page

Page

Page

LIST OF TABLES

Page

INTRODUCTION AND LITERATURE REVIEW

Internal Cooling

Internal cooling techniques for gas turbine blades have become increasingly important through recent years. Being able to properly cool the turbine blades allows for a higher rotor inlet temperature (RIT) which will result in an overall increase in thermal efficiency and power output from the engine. Figure 1 displays the increase in the inlet temperature of the gas turbine engine through recent decades. With great technological improvements in gas turbine blade cooling, the inlet temperature has increased to much higher than even the melting point temperatures of the metal blades.

In chapter four of Han et al. [1], internal cooling methods are presented in great detail. In terms of internal cooling, with three major cooling zones of the gas turbine blade (leading edge, mid-chord section, and trailing edge), many different cooling methods have been utilized to see which ones enhance heat transfer the greatest. It is understood in today's industry practices, that the leading edge is typically cooled by a jet impingement arrangement as shown in Figure 2. The trailing edge is typically cooled by pin-fins or dimpled surfaces and the mid-chord section is normally cooled by serpentine rib-roughened coolant passages. Jet impingement methods have also been used in the mid-chord section of the blade as well as shown in Figure 3. These heat transfer enhancement techniques can be used in many more applications in addition to just turbine blade cooling. Combustor liner cooling, electronic cooling, and even solar collector cooling can all use these techniques to aid in heat transfer. The focus of this

study will be to investigate a combination of these cooling techniques and simulate the conditions of non-rotational (stator) heat transfer in the mid-chord region of the gas turbine blade.

Rib-Turbulated Cooling

In chapter four of Han et al [1], a detailed discussion of rib-turbulated cooling is presented. In terms of rib-turbulated cooling, repeated rib turbulators (or ribs) are cast on internal walls in order to enhance heat transfer. Thermal energy conducts from the external side of the blade to the internal zones and the conducted heat is cooled by cooling air. Han [2] recognized that the heat transfer performance for a non-rotational ribbed channel depends mostly on the channel aspect ratio, the rib configuration, and the flow Reynolds number. One of the main attractions of rib-turbulated cooling and some of the main fundamental studies performed is to understand the flow separation that occurs as a result of the rib arrangement and incoming cooling flow. Depending upon the height of the rib and the rib spacing (pitch), the flow separation can separate and re-attach itself before hitting the next rib (see Figure 4). The resulting vortices and turbulent flow can increase heat transfer near the ribbed region. The downfall to this approach is observably the pressure drop that occurs across the region.

Han [3] investigated the effect of rib spacing on the heat transfer coefficient. The results indicated that as the pitch to height (P/e) ratio (see Figure 5) increased, the heat transfer coefficient decreased. Han et al. [4] studied the effect of different high performance rib configurations. The results indicated that the heat transfer coefficient increased with the rib arrangements however, the pressure drop also increased. It was

also shown that as the Reynolds number increased, the heat transfer coefficient decreased which indicates that the improvement of heat transfer with ribs decreases with increasing Reynolds number. Rallabandi et al. [5] studied heat transfer enhancement inside of a rectangular channel with axial ribs. The results indicated the heat transfer increased due to the increased surface area that the ribs provided as well as the turbulence induced by the ribs that cause the flow to separate and reattach itself.

In terms of rib roughen surface configurations, many studies have been performed to determine which alignment of the ribs with respect to the flow produces the highest heat transfer coefficients. Han and Park [6] investigated the heat transfer enhancement effects of the rib angle of attack with respect to the incoming flow. It was concluded that the angled ribs configurations had higher centerline Nusselt number ratios after reaching the fully developed periodic distribution, than the case of an orthogonal rib configuration. Also, the angled rib configurations had an increasing centerline Nusselt number ratios after the fully developed region due to the secondary flow behavior produced after hitting the ribs at an angle. Han and Zhang [7] studied the effects of continuous and broker ribs as well as parallel and V-shaped ribs. Continuous ribs refer to the type of rib that extends across the width of the channel. Broken ribs do not extend to the whole width of the channel and are also broken in the middle. The results indicated that the ribbed-side surface Nusselt number ratios for 60° and 45° broken ribs are much higher than the continuous ribs. The friction factors were relatively the same with the continuous ribs and broken ribs.

Pin-Fin Cooling

Pin-Fin cooling is also presented in great detail in chapter four of Han et. al [1]. Pin-fins (or pins) are round extrusions that are attached to the cooling surface in order to increase the surface area which ultimately increases heat transfer coefficient. The pins are usually attached perpendicular to the flow direction so that convection can be maximized. The wake shed by each pin increases the free-stream turbulence and the resulting vortices will increase heat transfer coefficient. Horseshoe vortices also originate upstream at the base of the pin causing flow disturbances around the pin. This in turn, increases the overall pressure drop across the channel. Pin-fins are usually installed on the trailing edge portion of the gas turbine blade due to the limitations of using rib turbulators or jet impingement in that region and ordinarily span the entire channel from wall to wall.

One important observation with pin-fin cooling is the gradual increase of Nusselt number near the inlet of the channel as opposed to the conventional smooth channel case. For the smooth channel case, the Nusselt number is highest near the start of the thermal boundary layer and decreases until the flow gets to the fully developed region. With the pin-fin array arrangement however, the first row of pins have a high localized Nusselt number but the flow gradually increases until the fully developed region. This is due to the horseshoe vortices that are created after the flow strikes the first row of pins and proceeds to the following row. Since the turbulence increases as the flow proceeds to the following rows, the localized Nusselt number gradually increases.

Chyu, M.K. [8] studied the effects of inline pin-fins arrangements versus staggered pin-fin arrangements. The results indicated that although both cases produced high Sherwood numbers (another parameter that describes heat transfer enchantment), the staggered case had slightly higher values. Arora and Abdel-Messeh [9] studied the effect of half-pins that do not span the entire channel and that have tip clearances on one side. The results show that the local Nusselt number with the wall that has the pins attached to them is comparable to that of the case with the full pins. The wall that did not have any pins and was left smooth had lower local Nusselt number distribution. Arora and Abdel-Messseh also analyzed the friction factor that occurs across several different pin fin arrangements. The results indicated that the use of partial pins has a much lower pressure drop than the case with the full pins.

Jet Impingement Cooling

This method of internal cooling has the most significant impact of increasing local heat transfer coefficient. The primary reason why this method of cooling is used for the leading edge of the turbine blade is because of its effective local cooling and the high thermal loads of the leading edge portion. The downfall of this approach is the large associated pressure drop and the construction of the flow arrangement weakens the structural strength of the turbine blade. Since the structural strength of the stator is less demanding than that of the rotor, jet impingement is also a method applied in industry to the mid-chord or the stator blade section as well. It is well understood that the heat transfer coefficient on the targeted surface increases with increasing Reynolds number, decreasing jet-to-target spacing, or decreasing jet-to-jet spacing (Wright and Han [10]).

In addition to these three traits, Chupp et al. [11] also concluded that the surface curvature relative to the diameter of the jet also affects the surface Nusselt numbers. It is important to note that even with the high local enhanced heat transfer, the jet impingement method produces large pressure drops between the plenum before the air enters the nozzles and the cooling region after the flow leaves the nozzle.

There is an additional phenomenon that occurs with the jet impingement method of cooling and that is the cross-flow effect. For this experiment, since there is only one exit for the air flow to exhaust from, the jet impinging air flow builds up on the closed side of the channel and moves through the channel to the exhaust. This in turn can cause the jets to deflect the air flow resulting in improper impact on the surface. Florscheutz and Su [12] have investigated the effect of cross-flow on the Nusselt number. Based off of their results, the cross-flow contributes greatly in enhancing the convective heat transfer. The cooling by the jet onto the surface decreased due to the jet deflection and since the heat transfer coefficient of the jet impingement is higher than that of the cross-flow, the overall heat transfer coefficient decreased. Huang et al. [13] investigated the effect of cross-flow direction on the impingement heat transfer. Three different configurations were studied: the spent air exiting from the furthest end relative to the entrance, the spent air exiting from both directions, and the spent air exiting from the nearest exit to the inlet. The results indicate that the cross-flow effect was significantly reduced with the cases that had exits in two directions. The third configuration produced a stronger cross-flow than the first configuration resulting in a lower peak Nusselt number.

Compound Cooling Techniques

Several studies have been performed to analyze the combination of several cooling techniques. Haiping et al. [14] performed an experiment simulating the mid-chord region of the turbine blade using a combination of jet impingement and rib turbulators. The study was performed to determine the effects of the jet impingement holes with respect to the rib turbulator location. Results indicated that impingement between the ribs provided the highest Nusselt number values. Rallabandi et al. [5] studied the effect of ribs on jet impingement application with rectangular channel. The results indicated that the axial ribs have an adequate impact on impingement heat transfer which is mainly the result of the increased surface area. The enhancement was not much more than the case without any roughened surface at all. The jet impingement cases that were performed also showed that the jet impingement provided much higher heat transfer enhancement than the channel flow case at the cost of higher pressure drop.

Trabold and Obot [15] investigated the effect of cross-flow on the impingement heat transfer with the use of rib turbulators. The experiment was performed with two different flow schemes which were with two exits and one exit. For the case of one exit flow scheme, the Nusselt numbers for the smooth case were slightly higher than those of the roughened surface case near the entrance region. The presence of the ribs reduced the heat transfer enhancement capabilities of the jet impingement in some areas. The smooth case had higher heat transfer near the closed end due to less cross-flow effect. The addition of the ribs reduced the heat transfer in that region. However, the heat transfer with the ribs increased downstream due to the separation and reattachment of the flow.

Finally, Azad [16] investigated the use of pin-fins on a jet impingement surface. In his experiment, many pins were used and were placed in an inline configuration with the jets at different exit conditions. The results indicated that the average Nusselt numbers were higher than the ribbed channel case from Trabolt and Obot [15].

EXPERIMENTAL PROCEDURE AND INSTRUMENTATION

With all of these various cooling techniques, research was carried out to see if any combinations of these methods can produce even greater thermal performance. Thus, for the channel flow setup, combinations of rib turbulators as well as pin-fins were studied to see if the performance can be enhanced. For the jet impingement setup, combinations of three of the cooling methods were implemented: jet impingement, rib turbulators, and pin-fins. Since pin-fins require less surface area and are lighter than the rib turbulators, if a higher thermal performance can be obtained, it can be ideal for future applications. The pin-fins that were utilized were partial pins that did not extend from wall to wall in the channel. This was because these experiments were performed simulating the conditions of the mid-chord region of the gas turbine blade. Table 1 below displays the different tests that were performed for this experiment.

Table 1 – Experimental cases to be performed.

Channel Flow Steady State Heat Transfer Experiment	**Jet Impingement Steady State Heat Transfer Experiment**
Smooth	Smooth
Only Rib Turbulators P/e Ratio of 10	Only Rib Turbulators P/e Ratio of 10
Only Rib Turbulators P/e Ratio of 5	Only Rib Turbulators P/e Ratio of 5
Only Pin-Fins P/e Ratio of 10	Only Pin-Fins P/e Ratio of 10
Only Pin-Fins P/e Ratio of 5	Only Pin-Fins P/e Ratio of 5
Combination of Rib Turbulators and Pin-Fins P/e Ratio of 10	Combination of Rib Turbulators and Pin-Fins P/e Ratio of 10
Combination of Rib Turbulators and Pin-Fins P/e Ratio of 5	Combination of Rib Turbulators and Pin-Fins P/e Ratio of 5
Combination of Rib Turbulators and Pin-Fins P/e Ratio of 2.5	Combination of Rib Turbulators and Pin-Fins P/e Ratio of 2.5

Each of the cases was performed at four different Reynolds number to investigate the effect of Reynolds number on the different configurations as well. The smooth case was performed in order to compare the results to previous experiments that were performed with the same experimental setup to ensure consistency with performing experiments with the setups.

The experimental facility has two main flow arrangements as shown in schematic of the test sections in Figure 6. Both the channel flow and jet impingement loops have entering cooling air provided from an air compressor. The incoming flow speed is adjusted via ball valves. In the upstream region of the flow (before entering either of the flow arrangements), the flow moves through an orifice plate so that the Reynolds number can be calculated. A static pressure gage is placed to read the static pressure of the incoming flow. Furthermore, a manometer is placed at the orifice meter in order to

measure the pressure drop across the orifice. The Reynolds number can then be calculated.

For the channel flow arrangement, after the flow travels across the orifice plate, the flow enters the channel passage. The channel flow passage consists of a uniform strip heater that is placed at the top of the channel. Under the heater, twelve equally sized copper plates are placed parallel to one another as shown in Figure 7. Copper plates are used because of the high thermal conductivity associated with them. Each copper plate has four thermocouples attached to them in between the heater and the plates. These thermocouples measure the local temperature of the copper plates and are averaged to get an overall temperature of each individual plate. The heater heats the copper plates with a specified power input and the air flows through the channel and cools the copper plates from the outside. Figure 8 displays the schematic for the channel flow passage. For this experiment, the copper plates were on top of the channel not below as shown in Figure 8. The flow entered the duct and went through a honeycomb structure in order to make the flow more uniform. Figure 9 shows the channel flow passage with the copper plates and the embedded thermocouples. Once the flow enters the heated section, convection takes place between the copper plates and the air. Thermocouples are also placed at the entrance and exit of the duct for monitoring the inlet and exit conditions as well. The flow is set to a specific Reynolds number and once the arrangement has reached steady state, data is recorded and the results are analyzed to see the heat transfer characteristics of the specific configuration of ribs and pins. For this experiment, only one channel aspect ratio was selected.

It is understood that with the channel flow configuration, a pressure drop of the flow occurs from when it first enters the plenum to when it exits. This pressure drop is associated with the friction caused between the surface and the incoming flow. Increasing the surface area with the use of rib turbulators and pin-fins will increase the associated pressure drop due to the friction increasing between the incoming flow and the roughened surface. Thus, eight static pressure taps are placed along the length of the channel and the static pressure is measured using an inclined manometer. Measuring the static pressure at these points allows for the friction factor to be calculated and see which configurations provide the greatest and least pressure drops across the channel.

In terms of the jet impingement configuration, after the flow travels across the orifice plate, the cooling air enters the jet impingement plenum. Figure 10 displays the schematic of the jet impingement setup. Three pressure taps are placed in the plenum area of the setup in order to record the pressure before the flow enters the nozzles. Two thermocouples are placed in the plenum area in order to monitor the inlet temperature conditions. Five thermocouples are placed at the end of the setup before the air flow exits to the atmosphere in order to record the exit temperature of the air. Figure 11 shows how the air enters and travels through the jet impingement setup. The flow enters from the bottom of the apparatus and again travels through a honeycomb structure similar to that of the channel flow arrangement in order to make the flow uniform. The flow enters the apparatus from the left side and right side in order to provide uniform flow through the jet holes. As the flow travels through the jet impingement holes, it strikes the copper plate surface and cools the plates. The same heater and copper plates that are used for the

channel flow setup are also used for this flow configuration as well. Since there is only one exit for the cooling flow to travel, the cooling air travels from the right to the left of the jet impingement passage creating a cross-flow affect. Figure 12 shows the arrangement and size of the jet impingement holes. The jet impingement apparatus also has several pressure taps along the length of the channel. Since there is a cross flow affect associated with the jet impingement setup, an inclined manometer is used to measure the pressure across the jet channel.

In terms of the copper rib and pin-fin configurations, only one angle of attack was selected which was 45° with respect to the incoming flow. The rib and pin-fin height were also the same. The parameters that changed were the P/e ratio as well as the amount of ribs/pin fins used. Figures 13-20 displays the different types of configurations that were used for the experiment. Finally, Table 3 in the Appendix provides a list of the instrumentation that was used for this experiment.

MEASUREMENT THEORY

The first step in determining the heat transfer coefficient for the flow configuration is to calculate the Reynolds number. In order to calculate Reynolds number, the mass flow rate is first calculated so that the velocity of the air can be determined. The procedure is outlined from Han and Wright [17]. The mass flow rate through the ASME square-edged orifice meter is given by:

$$w = SD_2^2 KY \sqrt{\left(\frac{p_1}{T_i}\right) Gy \Delta p} \tag{1}$$

In order to calculate the mass flow rate, the flow coefficient and the expansion factor must be determined. The flow coefficient is given by:

$$K = \frac{C}{\sqrt{1 - \beta^4}} \tag{2}$$

An iterative procedure must be performed in order to determine the flow coefficient. The details of how the flow coefficient can be calculated are provided from Fu [18] and are given in the Appendix section. The expansion factor is given by:

$$Y = 1 - \left[.41 + .35\left(\frac{D_2}{D_1}\right)^4\right]\left[\left(\frac{\Delta p}{p_1}\right)\left(\frac{1}{\kappa}\right)\right] \tag{3}$$

Equation (1) determines the mass flow rate in lbm/s. In order to proceed with the calculations, the mass flow rate is converted into metric units.

$$\dot{m} = \frac{w}{2.2} \tag{4}$$

After the mass flow rate is calculated, the velocity of the incoming air can be calculated with Equation 5 below.

$$V = \frac{\dot{m}}{\rho A_c} \tag{5}$$

Table 2.0 displays the different cross-sectional areas that were used for the different flow arrangements. The density is assumed to be constant for the air entering the test plenums with a value of 1.2 kg/m^3.

Table 2 – Cross-sectional area for the different flow arrangements.

Channel Flow Configuration	Jet Impingement Configuration
Length = 5in Width = 1in **A_c = 5in^2 = 0.003226m^2**	Based on jet hole diameter and total number of holes d_j = 0.25in Total number of holes = 48 **A_j= 2.356in^2 = 0.00152m^2**

The final step in determining the Reynolds number for the incoming flow is to determine the hydraulic diameter for the channel flow arrangement. In being consistent with previous literature, the Reynolds number for the jet impingement arrangement is based off of the jet hole diameter. For the channel flow configuration, the Reynolds number is based off of the hydraulic diameter which is given as:

$$D_h = \frac{4A_c}{P} \tag{6}$$

Since only one cross-section of the channel flow arrangement is being investigated for this experiment, the hydraulic diameter is 1.667in or 0.0423m. They Reynolds number for the channel flow and jet impingement configurations are defined as:

$$\mathrm{Re} = \frac{V \mathrm{D}_h}{\upsilon} \tag{7}$$

$$\mathrm{Re}_j = \frac{V \mathrm{d_j}}{\upsilon} \tag{8}$$

In terms of the heat transfer, the first objective in determining the Nusselt number for the flow configuration is to determine the head input load provided from the strip heater.

$$\dot{\mathrm{Q}} = \frac{\mathrm{V}^2}{\mathrm{R}} \tag{9}$$

The local heat flux can also be expressed as:

$$\mathrm{q}''_{\mathrm{w}} = \frac{\mathrm{q}}{\mathrm{A_p}} - \mathrm{q}''_{\mathrm{loss}} \tag{10}$$

After reading the voltage input into the heater and measuring the resistance across the heater, the heat load is determined. Once the heat load is known and the testing conditions reach steady state, the local wall temperature of the copper plates are known so that the heat transfer coefficient can be calculated.

In terms of the heat loss, a heat loss test can be performed in order to develop correlations for the amount of heat loss each copper plate produces. By placing insulation inside of the channel and turning on the heater on, the heat will be forced to transfer to the room environment. Once steady state has been reach without any air flow, the temperature difference can be recorded between the copper plates and the room. A

linear correlation can then be developed to estimate the heat loss for each copper plate. Since the heat loss only accounts for less than 5% of the overall heat transfer coefficient and since the correlations will not be much different if a new heat loss test is performed (under the same testing conditions), the correlations that were developed from Rallabandi et. al [5] are the same correlations that are used for this experiment (see Table 4 in the Appendix for the complete list). For the channel flow arrangement, after calculating the local bulk temperature associated with the incoming flow, the heat transfer coefficient can finally be calculated as:

$$h = \frac{q''_w}{T_w - T_B} \tag{11}$$

The local bulk temperature between each copper plate can be calculated in one of two ways. One method involves the linear interpolation between the inlet and exit air temperatures and the other method utilizes the energy equation which defines the local bulk temperature as:

$$T_e = T_i + \frac{\dot{Q}_{in} - \dot{Q}_{loss}}{\dot{m}c_p} \tag{12}$$

In this case, T_i represents the air temperature entering the region that is heated by a copper plate and T_e represents the exit temperature of the air from that region. The exit temperature for the first region will be the inlet temperature for the next region. The process is continued until eventually the exit temperature of the air from the setup is determined. The determined exit temperature can be compared with the measured exit temperature to see if the results are similar. If the results are not similar, than there is

error associated with the estimation of the heat loss. The bulk temperature that is calculated via the energy method can also be compared with the bulk temperature results determined from the interpolation method to compare accuracy. After determining the heat transfer coefficient for the channel flow steady state test, the Nusselt Number can finally be calculated and is given as:

$$\mathrm{Nu} = \frac{\mathrm{hD_h}}{\mathrm{k}} \tag{13}$$

An empirical Nusselt number can also be calculated that is based off of the enhancement in a smooth duct and is regulated by the Dittus-Boelter correlation which is defined as:

$$\mathrm{Nu_0} = 0.023\mathrm{Re}^{0.8}\mathrm{Pr}^{0.4} \tag{14}$$

Taking the ratio of the Nusselt number and empirical Nusselt number allows for a greater understanding of the enhancement effects for a certain flow configuration. It will not only be effective in comparing to previous literature but it gives the enhancement results based off of the actual Reynolds number that was measured for the certain flow configuration.

In terms of jet impingement calculations, the heat transfer coefficient is based off of the air flow inlet temperature as opposed to the bulk temperature since bulk temperature is only based on flow entering from one side of a channel. The heat transfer coefficient is defined as:

$$\mathrm{h} = \frac{\mathrm{q''_w}}{\mathrm{T_w} - \mathrm{T_i}} \tag{15}$$

The Nusselt number for the jet impingement is based on the jet hole diameter as opposed to the hydraulic diameter and is defined as:

$$\mathrm{Nu} = \frac{\mathrm{hd_j}}{\mathrm{k}} \tag{16}$$

It is understood that for the channel flow cases, pressure drop occurs across the flow channel. From Rallabandi et al. [5], once the pressure drop is measured via the static pressure taps, the Fanning friction factor can be estimated as:

$$\mathrm{f} = \frac{\mathrm{D_h}}{2\rho V^2}\left|\frac{\mathrm{dP}}{\mathrm{dx}}\right| \tag{17}$$

Similar to the heat transfer calculations, an empirical friction factor is defined that based off of the smooth case so that the friction factor of the roughened cases can be properly compared and analyzed. The empirical friction factor is normalized by the Swamee-Jain approximation as:

$$\mathrm{f_0} = \frac{0.331}{\ln\left(\frac{5.74}{\mathrm{Re}^{0.9}}\right)^2} \tag{18}$$

A thermal performance expression can be defined that compares the enhanced heat transfer with the pressure drop associated for a given flow configuration for the channel flow setup. It is defined as:

$$\mathrm{TP} = \frac{\mathrm{Nu}/\mathrm{Nu_0}}{(\frac{\mathrm{f}}{\mathrm{f_0}})^{1/3}} \tag{19}$$

Thus, the higher the thermal performance for a given flow configuration, the better it will be because that will indicate that the configuration provides high heat transfer for cooling, with little or less pressure drop.

Since there is a cross-flow affect associated with the jet impingement experiment, a percentage of cross-flow that accumulates in the channel can be

determined. The first step in calculating the percentage of cross-flow is to calculate the pressure difference between the plenum and the pressure in the jet channel. Since there are twelve jet holes along one row of the channel, linear interpolation is used to determine the pressure drop for the regions that do not have a pressure tap. After the pressure difference is calculated between the plenum pressure and the pressure in the twelve regions, the mass flow rate is calculated with the following equation which was provided from Liu et al. [19]:

$$\dot{m}_j = C_D A_j \left[\sqrt{2\rho(P_{Plenum} - P_e)}\right] \tag{20}$$

where the pressure terms are in units of Pascals. Since there are a total of four holes along the width of the channel, this mass flow rate value is multiplied by four in order to get the total mass flow rate at one region. Once the mass flow rate is calculated for all twelve regions and multiplied by four, the total mass flow rate through the 48 holes is measured by summing them all up. Furthermore, this mass flow rate is then compared with the mass flow rate that was measured through the orifice meter. An iterative procedure takes place in which the discharge coefficient changes until both mass flow rates are equal. After finalizing the discharge coefficient to make the mass flow rates equal, the percent of cross-flow can be calculated by Equation (21) which is provided from Florschuetz et al. [20].

$$\%\ \text{Cross Flow} = \frac{G_C}{G_j} = \frac{\frac{\sum \dot{m}_j}{\rho A_c}}{\frac{\dot{m}_j}{\rho A_j}} \tag{21}$$

where the velocity through a specific region of the channel is equal to the sum of all the mass flow rates before that region divided by the density and cross-sectional area of the channel.

Finally, since there are many uncertainties associated with this experiment, the second power equation is used to estimate these uncertainties. The second power equation is shown in Equation (22) below.

$$w_R = \left[\left(\frac{\partial R}{\partial v_1} w_1\right)^2 + \left(\frac{\partial R}{\partial v_2} w_2\right)^2 + \cdots\cdots\cdots\cdots \left(\frac{\partial R}{\partial v_n} w_n\right)^2\right]^{\frac{1}{2}} \qquad (22)$$

Where *v* represents the independent variables, *R* represents the function of the independent variable, and *w* represents the uncertainty interval.

RESULTS AND DISCUSSION

Channel Flow

The first set of experiments that were performed was the smooth configuration at different Reynolds numbers. The results were compared with previous literature to ensure that the experiential facility still worked suitably. Figures 21-24 display the results for the smooth case data at the different Reynolds numbers and comparing them with previous experiment performed by Rallabandi et al. [5]. The results indicate that the Nusselt number ratio is in fact similar in both cases at all of the different Reynolds numbers so the smooth case results can be used as reference when comparing the rough cases.

Figures 25-28 display the Nusselt number distribution for all of the different configurations for the channel flow setup at the four different Reynolds numbers. The results show that all of the cases provided local Nusselt numbers that were higher than the smooth case. In order to determine the amount of heat transfer enhanced compared to the smooth case, the Nusselt number was normalized by the Dittus-Boelter correlation and a Nusselt number ratio was calculated. The results are shown in Figures 29-32. Based off of the results, the highest heat transfer came from the all ribs configuration with a P/e ratio of 5. This is mainly due to the larger increase in surface area compared to the other cases, which significantly increased the heat transfer coefficient. Another cause of the high heat transfer is due to the increase in flow separation and re-attachment that is associated with the air flow over the rib turbulator. This resulted in an increase in

turbulence which also increased the heat transfer coefficient. The next case with the highest Nusselt number ratio was the case with a combination of rib turbulators and pin-fins with a P/e ratio of 5. Again, this is due to the higher surface area associated with this case compared to the other cases (such as those with P/e ratio of 10). All of the cases that had a P/e ratio of 10 which included: all ribs, all pins, and a combination of ribs and pins, had very similar Nusselt number ratios. Interestingly, the case of a combination of rib turbulators and pin fins with a P/e ratio of 2.5 had a significantly low Nusselt number ratio. It was hypothesized that the case with the largest increase in surface area would produce the highest localized heat transfer coefficients. The results indicate the Nusselt number ratio is similar to all of the cases that had a P/e ratio of 10. The utmost probable reason for the low Nusselt number ratio is due to the lack of proper flow separation and reattachment. All of the rib turbulators and pin-fins were too close to each other so that there was no room for proper separation which resulted in less turbulence.

In terms of the flow velocity affect on heat transfer for the channel flow setup, the higher the Reynolds number, the lower the heat transfer coefficients and corresponding Nusselt numbers and Nusselt number ratios. As shown in Figures 29-32, for the smooth case, the Nusselt number ratio stayed the same despite the increase in Reynolds number. The slight decrease in Nusselt numbers for the rough cases is due to the less penetration of the higher momentum fluid onto the roughened surface.

Figures 33-36 display the pressure drop across the channel for all of the cases at the different Reynolds numbers. The case with the highest pressure drop was the all ribs case with a P/e ratio of 5. Without any roughened surface, the smooth case had the least

frictional losses and resulting pressure drop. The all pins case with a P/e ratio of 5 had significantly lower pressure drop than the other cases that were at P/e ratio of 5 which is a good indication of overall thermal performance. In terms of the cases that had a P/e ratio of 10, the all ribs case again had the highest values and the all pins case had the lowest values with the case of ribs and pins lying in the middle. Contradictorily, the case with the combinations of ribs and pins with a P/e ratio of 2.5 had a very low pressure drop. The most likely reason for this is due to the lack of proper flow separation and reattachment. Since the pins and ribs are too close to each other, the flow does not have proper area to separate resulting in less turbulence being generated. Furthermore, with less turbulence, the pressure drop would be less.

Figure 37 displays the friction factor for the channel flow results at the different Reynolds numbers. The results indicate that for each case, the friction factor stayed nearly the same as the Reynolds number increased indicating that the pressure drop slopes stayed the same at the different Reynolds numbers for the various cases. Like the Nusselt number results, in order to determine how each case compared to the smooth case, the friction factor is normalized to an equation based off of the smooth case. Equation (18) was used to normalize the friction factor. This equation was compared to other relations that are well known in literature to check for consistency. Figure 38 displays the results of this comparison for the smooth case. The Swamee-Jain expression was compared to some relations that were curve fitted from the well known Moody diagram. The results indicate the Swamee-Jain approximation is accurate in calculating the friction factor based off of smooth case. Figure 39 displays the friction factor results

based off of the Swamee-Jain approximation. As the Reynolds number increased, the friction factor decreased indicating the results are consistent with literature.

Figure 40 shows the results of the friction factor ratio for all of the cases. It is understood that as the Reynolds number increased, the friction factor ratio also increased because the friction factor based off of smooth case decreased. The results indicate that the all ribs case with a p/e ratio of 5 had the highest friction followed close by the cases with ribs and pins with P/e ratio of 5 and 2.5. Interestingly, the case with only pins had the lowest friction factors with the exception of the smooth case. The all pins case with P/e ratio of 5 even had less frictional losses than all of the cases that involved ribs (either P/e ratio of 10 or 5). This provides potential for good thermal performance. Furthermore, for the smooth case, it can be said that when comparing the experimental friction factor to the empirical friction factor, the ratio shows that the value is greater than one. As the Reynolds number increased, the friction factor ratio also increased to some extent. This is due to the fact that the smooth surface is not perfectly smooth. There is some roughness associated with the smooth surface that trips the boundary layer and increases the turbulence in the flow. As the Reynolds number increased, the turbulence generated increased causing an increase in the friction factor.

Figure 41 displays the average Nusselt number ratio at the different Reynolds numbers. The first copper plate region and the last cooper plate region are not included in computing the average Nusselt number. Due to the thermal entrance region effect as well as unaccounted axial conduction, the Nusselt numbers for those two regions were higher than expected. Thus, they were omitted from the average Nusselt number

calculation. Based on the results, the all ribs case with a P/e ratio of 5 had the highest average Nusselt number at the different Reynolds number followed by the case of ribs and pins with a p/e ratio of 5. The rest of the cases with the exception of the smooth case had relatively close average Nusselt numbers at the different Reynolds number. Thus, this indicates that the thermal performance for these cases will be different since the friction factors were different. The average Nusselt number decreased as Reynolds number increased again due to the friction factor increasing at different Reynolds numbers.

Figure 42 displays the thermal performance results for the channel flow cases at different Reynolds numbers. The highest thermal performance was provided from the case of all ribs with a P/e ratio of 5. Even though the pressure drop was higher than all of the other cases as well, the heat transfer associated with this case was so high, that it still had the best overall thermal performance of an average of about 1.7. The second case with the highest overall thermal performance was the case of ribs and pins with a P/e ratio of 5. Interestingly, this case had a very close overall thermal performance to the case of all pins P/e ratio of 10. The all pins P/e ratio of 10 case had a very good overall thermal performance considering the fact that it utilizes much less material than the previous two cases and provides much less pressure drop. Even though the heat transfer enhancement was not as high as the previous two cases, the small pressure drop makes up for that. The other great result from this case is that the thermal performance is even better than the case of all pins P/e ratio of 5. Thus, utilizing less number of ribs and pins in the V-shape configuration can provides overall better performance for channel flow

applications. The case of ribs and pins with P/e ratio of 5 had a very close thermal performance to the case of P/e ratio of 10 but it was slightly lower. The all ribs case and ribs and pins case of P/e ratio of 10 had relativity low overall thermal performance indicating that there heat transfer enhancement that they provided did not compensate enough for the high pressure loss associated with them. Finally, the ribs and pins case with P/e ratio of 2.5 had a very bad overall thermal performance which was close to the performance of the just smooth case. Since it did not significantly enhance heat transfer due to the lack of proper flow separation, and higher pressure drop than the smooth case as well, allowed its thermal performance to be low.

The thermal performance factor in general is a measure of the configuration's ability to enhance heat transfer at the cost of overcoming the pressure losses. The fact that the friction factor ratio is raised to the one-third power (as shown in Equation (19)) while the Nusselt number ratio is not indicates that there needs to be three times as much pumping power for the air to overcome the losses in order to get the desired heat transfer results. So for the smooth case which had a thermal performance factor of about one, the power output in terms of heat transfer comes at the cost of about three times as much pumping power to overcome the pressure losses. Also, the thermal performance decreased for all of the cases as the Reynolds number increased due to the increase in friction factor ratio as the Reynolds number increased.

The previous results were all based on the smooth surface area which did not include the additional surface area of the roughened surfaces. The calculations were performed in order to analyze the overall heat transfer enhancements based on a

projected area to see which provides the greatest heat transfer coefficients. Thus, the heat transfer results would be attributed to the increase in surface area as well as the turbulence induced by the flow configuration. Another parameter to evaluate is the heat transfer affects based on the total surface area of the surface. Hence, this consideration gives a greater understanding on the effect of turbulence on the overall heat transfer enhancement. Figure 43 displays the average Nusselt number ratio based on the total area for the given flow configuration. Table 7 provides the details of each case and how much surface area was increased for the particular case. Also provided, is the percentage attributed to the increase in surface area using rib turbulators as well as the pin-fins for any specific configuration. As shown in Table 7, for all of the cases in which a combination of ribs and pins were used, the ribs attributed to about 57% of the increased surface area whereas the pins utilized about 43%. As expected, for the P/e ratio of 10 cases, the largest increase in surface area is attributed to the case of all ribs, followed by the case of ribs and pins, and finally the case of all pins. The same applies for the cases of P/e ratio of 5. The case with a combination of ribs and pins with a P/e ratio of 2.5 had an overall increase in surface area of about 87% indicating that the entire surface was almost doubled from the original surface.

Based on Figure 43, it can be said that the highest overall heat transfer enhancement based on the total area can be given to the case of all ribs P/e ratio of 5. All of the cases that had a P/e ratio of 10 had relatively the same average Nusselt number ratio based on total area indicating that the turbulence created in all three of the cases, produced similar heat transfer enhancements. In terms of the P/e ratio of 5 cases, the all

pins configuration had less heat transfer enhancement than the other cases that utilized ribs indicating the use of rib turbulator provides a means of producing greater turbulence. Finally, it should be noted that the case of a combination of ribs and pins with a P/e ratio of 2.5 produced a very low average Nusselt number ratio based on total area. The results are in fact very similar to the smooth case results. This again is a result of the fact that there is not a great turbulence effect with this case due to the lack of proper flow separation. The pins and ribs are so close to each other that the flow does not separate properly and thus, the only heat transfer enhancement that takes place is due to the increase in surface area. All of the other cases produced average Nusselt number ratios greater than the smooth case indicating that turbulence plays a major role in the heat transfer enhancing effects.

Figure 44 displays the thermal performance for the channel flow results based on the total surface area. These results indicate which case provides the best overall performance based on the turbulence produced and does not account for the increase in surface area. Interestingly, the overall thermal performance is attributed to the case of all pins and P/e ratio of 10.

Jet Impingement

Like the channel flow setup, the first set of experiments performed on the jet impingement setup was the smooth case configuration at different Reynolds numbers. The results were compared to previous literature performed with the same apparatus to ensure that the results remain consistent. Figures 45-48 display the Nusselt numbers for the smooth case at the different Reynolds numbers along with the Nusselt numbers from

the previous test performed by Rallabandi et al. [5]. The figures indicate that the local Nusselt numbers are about 20% lower than the previous results but the overall trend is the same. Since the trend is the same, it indicates that the calculations were performed correctly. The error can come from either differences in power input, differences in room temperature and wall temperatures (from proper calibration), or the heat loss. The heat loss was calculated using the same correlations that were used for channel flow setup. Depending upon the amount of insulation that was used in the previous experiment, the results can slightly vary.

Figures 49-52 display the local Nusselt number distribution for the jet impingement cases at the different Reynolds numbers. First and foremost, it can be said that as the Reynolds number increased, the heat transfer coefficients increased and thus, the local Nusselt numbers increased. Furthermore, it can be concluded that none of the roughened cases had any significant heat transfer enhancements when comparing the results to the smooth case. For the 5000 Reynolds number cases, most of the cases produced an overall higher local Nusselt number distribution than the smooth case. However, at the higher Reynolds numbers, most of the cases had overall lower local and average Nusselt numbers than the smooth case. All of the cases followed a similar trend as the flow moved downstream. As x/d increased, the local Nusselt number decreased until it leveled out. The heat transfer in the entrance region is higher due to less cross flow effect on the jets. As the cross-flow increased, the air flow jets became bent and had less impact on the test surface. After x/d of about 20, the Nusselt number leveled even though the cross flow had greater impact downstream. This is because the further

downstream the air traveled, the more like channel flow it behaved in which additional turbulence was created as the flow traveled past the smooth and roughened surfaces.

Figure 53 displays the average Nusselt number for the cases at the different Reynolds numbers. Like the channel flow case, the first and last regions are omitted from the calculation of the average Nusselt number due to entrance region losses and unaxial conduction. Based off of the figure, it can be concluded again that for each Reynolds number, the cases all produced Nusselt numbers in the same range. In order to get a better idea of which case performed better, a Nusselt number ratio calculation was performed for all of the cases. In order to determine the proper empirical Nusselt number relation for the jet impingement setup, the data for the smooth case was compared to empirical relations from literature to see if to see if any of the smooth case data can match the expressions. Figure 54 displays the average Nusselt numbers for all of the cases along with a few empirical relations. The smooth case came close to one of the correlations developed by Huang et al. [13] but it did not match exactly the same. It came closer to the relation developed by Kercher and Tabakoff (see Huang et al. [13]) but they were still considerably different. Thus, a new correlation was developed for the smooth case by curve fitting the results from Figure 54. The resulting empirical Nusselt number expression ($Nu_0=0.049Re^{6948}$) was compared with the average Nusselt numbers for the roughened cases and the Nusselt number ratio was plotted in order to compare the rough cases to the smooth case as well as correct for differences in Reynolds number.

The average Nusselt number ratio for each of the cases was calculated and the results are shown in Figure 55. It can be concluded that the rough cases enhanced heat

transfer better at lower Reynolds numbers than the higher ones. Also, the cases with all ribs provided the least heat transfer enhancement of all the cases followed by the cases with ribs and pins. The cases that had the best enhancement were the cases with only pin-fins. One explanation for this is to consider the amount of surface area that is being added by the ribs. Although increasing the surface area of the target surface generally increases the heat transfer coefficient, this can lead to less direct contact on the surface by the impinging flow. In addition, since the ribs were at a 45° angle, many of the jet holes could have directly impinged on the rib instead of the jet surface which would not enhance heat transfer as good due to the extra conduction. The pins provided more area of the surface to still get directly impinged by the incoming flow.

In terms of heat transfer enhanced by additional turbulence of the rough cases, the average Nusselt number for all of the cases was plotted based off of total area. The results are shown in Figure 56. When considering the Nusselt numbers based on total area, all of the cases fall below the smooth case. In addition, the case with the highest increase in surface area (i.e. Ribs and Pins P/e ratio of 2.5) had the lowest average Nusselt number which indicates that much of the enhancement that was produced in this case was by the increase in surface area and not much by additional turbulence being produced. Likewise, all of the cases that had P/e ratio of 5 had lower average Nusselt number values due to the large increase in surface area. The best case was the all pins case with a P/e ratio of 10.

The cross-flow percentage was calculated for the test section in order to understand its effect on the experiment. The results for the cross-flow percentage for all

of the different cases are presented in Tables 8-15 in the Appendix. The results are also plotted for the four different Reynolds numbers and the results are given in Figures 57-60. Based on the results, it can be said that the overall cross-flow percentage near the exit of the channel was a little over 40% for all of the cases. This indicates that the cross-flow had a significant impact on the heat transfer downstream. The cross-flow causes the jet beams to bend and avoid direct contact with the test surface resulting in lower Nusselt numbers as the flow progressed downstream. This also explains why the local Nusselt numbers started to increase again at the end of the channel. The high cross effect started increasing the local heat transfer coefficients causing the local Nusselt numbers to increase in the far end regions.

Overall Comparison

Based on the results, as the Reynolds number increased, the heat transfer decreased for the channel flow experiment but increased for the jet impingement experiment. For the channel flow setup, this is due to less flow separation at higher Reynolds number. For the jet impingement setup, the increasing heat transfer enhancement as a result of increasing Reynolds number is due to the greater impact of the incoming air at higher velocity on the test section. Figure 61 displays the combined heat transfer coefficients of the channel flow setup as well as the jet impingement setup as a function of the total mass flow rate entering the channels. Figure 62 displays the pressure drop across the channel flow setup as well as the jet impingement setup as a function of the total mass flow rates entering. Based on the results, it can be clearly seen that the jet impingement offers higher heat transfer coefficients over the same mass flow

rates of the channel flow at the cost of a much higher pressure drop with the exception of two of the channel flow cases. For the channel flow cases of all ribs P/e ratio of 5 and ribs and pins P/e ratio of 5, the heat transfer coefficients are higher with the same amount of total mass flow rate entering the jet impingement configuration. Although the jet impingement heat transfer results are lower than previous studies performed, the high heat transfer coefficients for these two channel flow cases is a good indication that they enhance heat transfer greatly. Particularly the ribs and pins case with a P/e ratio of 5 which even saves on area compared to the all ribs case of P/e ratio of 5. Furthermore, the rough cases provided different ranges of heat transfer coefficient distribution for the channel flow setup whereas for the jet impingement setup, they all produced values in the same range.

Uncertainty and Error

There were several sources of uncertainty and error in this experiment. Sources of random uncertainty include: slight fluctuations in power input to the heater from the variac, the air flow conditions for the air compressor being at different inlet temperatures, the quality of the air coming from the compressor (depending upon the amount of oil particles) which could slightly affect the air density and thermal conductivity, the room temperature changing throughout the experiments, and some probable small areas of leakage in the test channel in a few areas. However, these errors were very insignificant in impacting the results and are all less than 5%.

Types of systematic uncertainty include: the thermocouples calibration procedure (the accuracy of thermocouples), calibration of the incline manometer to the zero

marker, the reading of the inclined manometer, pressure regulation for the flow entering the orifice (trying to maintain the same inlet pressure and pressure drop across the orifice for all of the cases), heat loss correlations being slightly off, minor fluctuations with the digital multimeter, and the accuracy of the terminal block. Table 3 displays the percent error involved with the instruments used for the experiment. Table 4 displays the calculated relative uncertainties using the second power equation, for all for all of the different Reynolds number cases for both channel flow and jet impingement experiments. The low Reynolds number channel flow setup had the highest relative uncertainly due to the reading of the pressure gage at excessively low pressures. As the Reynolds number increased, the uncertainty decreased due to the inaccuracy of the instruments having less effect at higher pressures.

Table 3 – Percent error for experimental instruments.

Error Type	**Percent Error**
Thermocouples	0.20%
Pressure Gage	1.00%
Pressure Gage Reading	2.50%
Manometer	1.00%
Manometer Reading	0.25%
Digital Multimeter	0.01%
National Instruments Terminal Block	1.63%-2.50%

Table 4 – Relative uncertainties for channel flow and jet impingement cases.

	Mass Flow Rate	Reynolds Number	Heat Transfer Coefficient	Nusselt Number	Friction Factor
Re=10K (Channel)	25.89%	26.56%	5.690%	6.430%	27.60%
Re=20K (Channel)	8.860%	10.65%	5.420%	6.190%	10.82%
Re=30K (Channel)	6.400%	8.720%	5.410%	6.190%	8.930%
Re=40K (Channel)	5.580%	8.130%	5.420%	6.190%	8.150%
Re=5K (Jet)	11.13%	12.61%	5.390%	6.170%	-
Re=10K (Jet)	6.120%	8.510%	5.400%	6.170%	-
Re=15K (Jet)	5.360%	8.370%	5.400%	6.170%	-
Re=20K(Jet)	5.160%	7.850%	5.380%	6.160%	-

CONCLUSIONS

In conclusion, compound cooling techniques are a very effective means of enhancing heat transfer throughout many heat transfer applications. In terms of the mid-chord region for the gas turbine blade, utilizing some of these methods can provide overall greater heat transfer enhancements while saving on additional cost and weight.

For the channel flow setup, flow entered a 5”x1” channel at different Reynolds numbers. With a total of eight different configurations (seven rough surfaces and one smooth), steady state heat transfer tests were performed to see which configuration would enhance the heat transfer test the best. The following conclusions can be made based off of this experiment.

1) All of the rough cases enhanced heat transfer when comparing to the smooth surface.
2) Based on average Nusselt number, the cases that had larger surface area produced higher heat transfer (with the exception of the 2.5 ratio case due to improper flow separation).
3) The all ribs case with a P/e ratio of 5 produced the highest heat transfer coefficients but it also produced the highest friction factor for the flow. The resulting thermal performance was also the highest but when taking into account the total surface area increase; it was not the best performer.
4) Both of the cases with only pins produced very low pressure drop penalties when compared to the cases that utilized ribs. This is due to the fact that since

the pins have air gaps in between them, the flow can flow easier around the pins whereas with the ribs, the flow will be more disturbed. The low pressure drop also translates into the overall thermal performance being comparatively high for these two cases when compared to the other cases.

5) The ribs and pins case of P/e ratio of 5 is the best candidate for high heat transfer cooling. In terms of the thermal performance, it was almost as good as the all ribs case of P/e ratio of 5 but the amount of area saved is roughly 7%. This can save additional weight which would make the turbine blade lighter and thus, more efficient.
6) If taking into account the total surface area, the case of all pins with a P/e ratio of 10 is the best performer. It produced the least pressure drop with the exception of the smooth case. The average Nusselt numbers were not as high as a few of the other cases but the thermal performance and specifically the thermal performance based on total area, makes it the best candidate.

In terms of the jet impingement experiment, flow entered a plenum that had jet holes at the end of it. The jet holes ejected air from 48 holes onto a test surface which was made up of the same eight configurations (seven rough and one smooth). The following conclusions can be made for the jet impingement experiment:

1) The average heat transfer coefficients were higher for the jet impingement runs than the channel flow runs with the exception of two channel flow cases. The high heat transfer for the jet impingement cases is principally due to the direct impingement on the test surface.

2) None of the roughened cases enhanced heat transfer greater than the smooth case overall with the exception at the low Reynolds number of 5000. There can be some error involved but roughened surfaces do not generally enhance heat transfer by a great amount for jet impingement configurations when comparing to the smooth configuration.
3) The case of all pins P/e ratio of 5 performed the best of all the roughened cases. This is due to the fact that since the pins are discontinuous along the V-shaped profile, the air can directly impinge on the surface in more areas.
4) The case of all pins P/e ratio of 10 can save on increasing area anywhere from between 3-50% when comparing it to the other cases that did not perform as well. This provides an immense weight savings factor when designing the internal cooling structure of the gas turbine blade. In addition, this case also performed the best when taking into account the total area.
5) Cross-flow had a significant contribution to the heat transfer results. In all of the cases, the cross-flow got up to about 43% as the flow traveled downstream. The results lowered the heat transfer coefficients downstream due to the bending of the jet beams but started increasing locally towards the end due to the cross-flow heat transfer.

Finally, when comparing the channel flow cases to the impingement cases, two of the channel flow cases provide higher heat transfer coefficients when considering the same total mass flow rates of the impingement cases which is exceptional considering that all of the impingement cases produced higher pressure drops across the channel.

FUTURE RESEARCH

The future steps for this research can involve taking the compound cooling techniques to an even greater level. For example, another type of material that has been investigated for enhancing heat transfer in a channel is metal porous material. The porous material which can be used as an alternative to the copper plates drastically increases the surface area of the test section. Also, since the material is very rough, the turbulence produced is considerably high. As a result, the heat transfer enhancements are exceptional. Combining this porous material with a combination of rib turbulators and pin-fins can potentially maximize the amount of heat transfer that can take place in a channel. Also, using a combination of the porous material, ribs, pins-fins, and the jet impingement method is another compound cooling technique that can take the results to the maximum limit of how much enhancement this type of compound cooling technique can produce.

REFERENCES

[1] Han, J.C., Dutta, S., and Ekkad, S.V., 2013, *Gas Turbine Heat Transfer and Cooling Technology*, Taylor and Francis, Inc, New York.

[2] Han, J.C., 1984, "Heat transfer and friction in channels with two opposite rib-roughened walls," ASME Journal of Heat Transfer, **106**, pp. 774-781.

[3] Han, J.C., 1988. "Heat transfer and friction characteristics in rectangular channels with rib turbulators," ASME Journal of Heat Transfer, **110**, 321-328.

[4] Han, J.C., Zhang, Y.M., and Lee, C.P., 1991, "Augmented heat transfer in square channels with parallel, crossed, and V-shaped broken ribs," ASME Journal of Heat Transfer, **113**, 590-596.

[5] Rallabandi, A.P., Rhee, D.H., Gao, Z., and Han, J.C., 2010, "Heat transfer enhancement in rectangular channels with axial ribs or porous foam under through flow and impinging jet conditions," International Journal of Heat and Mass Transfer, **53**, 4663-4671.

[6] Han, J.C. and Park, J.S., 1988, "Developing heat transfer in rectangular channels with rib turbulators," International Journal of Heat and Mass Transfer, **32**(9), 1619-1630.

[7] Han, J.C. and Zhang, Y.M., 1992, "High performance heat transfer ducts with parallel broken and V-shaped angled ribs," ASME Journal of Heat and Mass Transfer, **35**(2), 513-523.

[8] Chyu, M.K., Hsing, Y.C., and Natarajan, V., 1998b, "Heat transfer contributions of pins and endwall in pin-fin arrays: Effects of thermal boundary condition modeling", International Gas Turbine & Aeroengine Congress & Exhibition, Stockholm, Sweden, June 2-5, ASME Paper 98-GT-175.

[9] Arora, S.C. and Abdel-Messeh, W., 1989, "Characteristics of partial length circular pin fins as heat transfer augmenters for airfoil internal cooling passages," Gas Turbine and Aeroengine Congress and Exposition, June 4-8, Toronto, Ontario, Canada, ASME Paper 89-GT-87.

[10]Wright, L.M., and Han, J.C., 2013, "Heat transfer enhancement for turbine blade internal cooling," Summer Heat Transfer Conference, July 14-19, Minneapolis, MN.

[11]Chupp, M.K., Helms, H.E., McFadden, P.W., and Brown, T.R., 1969, "Evaluation of internal heat transfer coefficients for impingement cooled turbine airfoils," AIAA Journal of Aircraft, **6**, 203-208.

[12]Florschuetz, L.W. and Su, C.C., 1987, "Effects of crossflow temperature on heat transfer within an array of impinging jets," ASME Journal of Heat Transfer, **109**, 74-82.

[13]Huang, Y., Ekkad, S.V., and Han, J.C., 1998, "Detailed heat transfer distributions under an array of orthogonal imping jets," AIAA J. Thermophys. Heat Transfer, **12**(1), 73-79, 1998.

[14]Haiping, C. Dalin, Z., and Taiping, H., 1997, "Impingement heat transfer from rib roughened surface within arrays of circular jet; The effect of relative position of the jet hole to the ribs," International Gas Turbine & Aeroengine Congress & Exhibition, June 2-5, Orlando, FL,ASME Paper 97-GT-331.

[15]Trabolt, T.A., and Obot, N.T., 1987, "Impingement heat transfer within arrays of circular jets. Part II: Effects of crossflow in the presence of roughness elements," Gas Turbine Confrence & Exhibition, Anaheim, CA, May 31-June 4.

[16]Azad, G.M., Huang, Y., and Han, J.C., 2000a, "Jet impingement heat transfer on pinned surfaces using a transient liquid crystal technique," Proceedings of the 8th International Symposium on Transport Phenomena and Dynamics of Rotating Machinery, Honolulu, HI, **2**, pp.731-738.

[17]Han, J.C., and Wright, Lesley, 2012, *Experimental Methods in Heat Transfer and Fluid Mechanics*, Texas A&M University, College Station, Texas.

[18]Fu, Wen-Lung, "Flow Rate Measurement: Using Thin-Plate Orifice with Square-Edged," 2002, Texas A&M University.

[19]Liu, Y., Huh, M., Wright, L., and Han, J.C., 2008, "Heat Transfer in Trailing Edge, Wedge Shaped Cooling Channels with Slot Ejection under High Rotation Number," Proceedings of ASME Turbo Expo 2008: Power for Land, Sea and Air, Berlin, Germany, June 9-13, GT 2008-50343.

[20]Florschuetz, L.W., Truman C.R., and Metzger D.E., 1981. Streamwise flow and heat transfer distributions for jet array impingement with crossflow. ASME Journal of Heat Transfer, **103**, 337-372.

[21]Sautner, M., Clouser, S., and Han, J.C., 1992, "Determination of surface heat transfer and film cooling effectiveness in unsteady wake flow conditions," AGARD Conference Proceedings, **527**, pp. 6-1-6-12.

[22]Han, J.C. and Rallabandi, A.P., 2010. Turbine blade film cooling using PSP technique. Frontiers in Heat and Mass Transfer, **1**(1),1-21.

[23]Han, J.C., and Wright, L., "Enhanced Internal Cooling of Turbine Blades and Vanes," Powerpoint Presentation.

APPENDIX

FIGURES

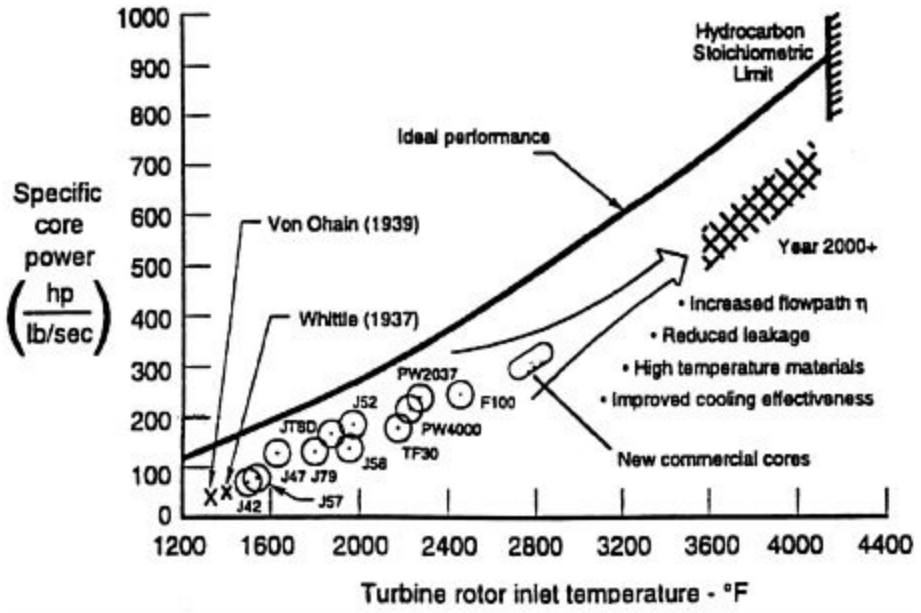

Figure 1 – Gas turbine inlet temperature increase throughout recent decades. Provided from Sautner et al. [21].

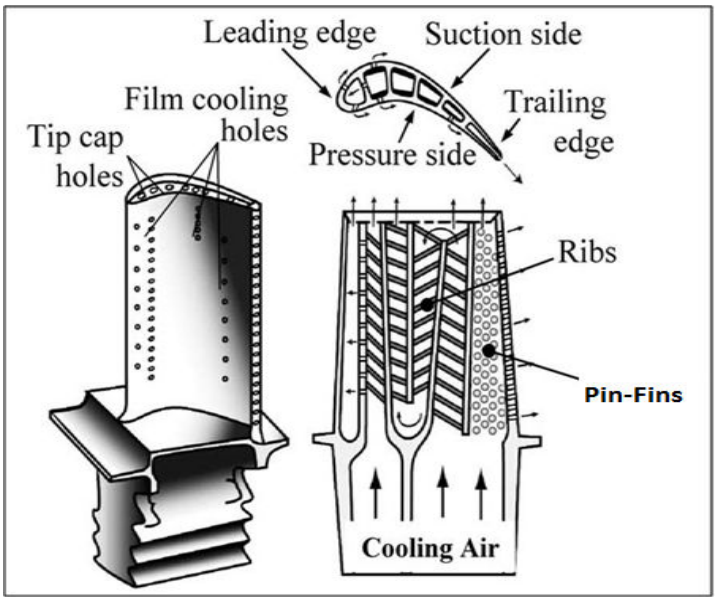

Figure 2 – Illustration of cooling techniques for the gas turbine blade. Provided from Han and Rallabandi [22].

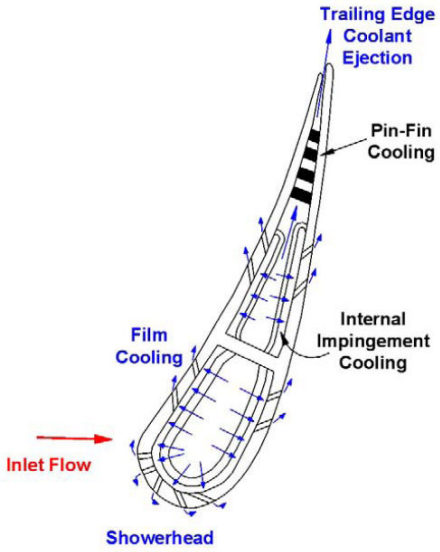

Figure 3 – Illustration of various internal cooling techniques for the gas turbine blade. Provided from Han and Wright [23].

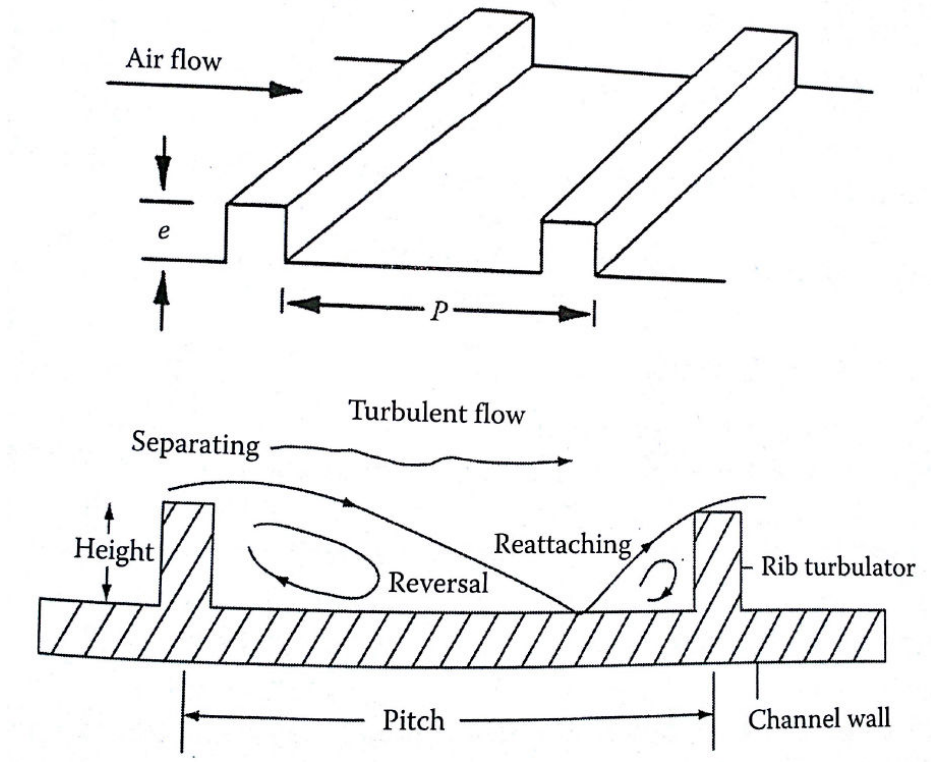

Figure 4 – Rib-turbulated cooling fundamentals. Provided from Han et al. [1].

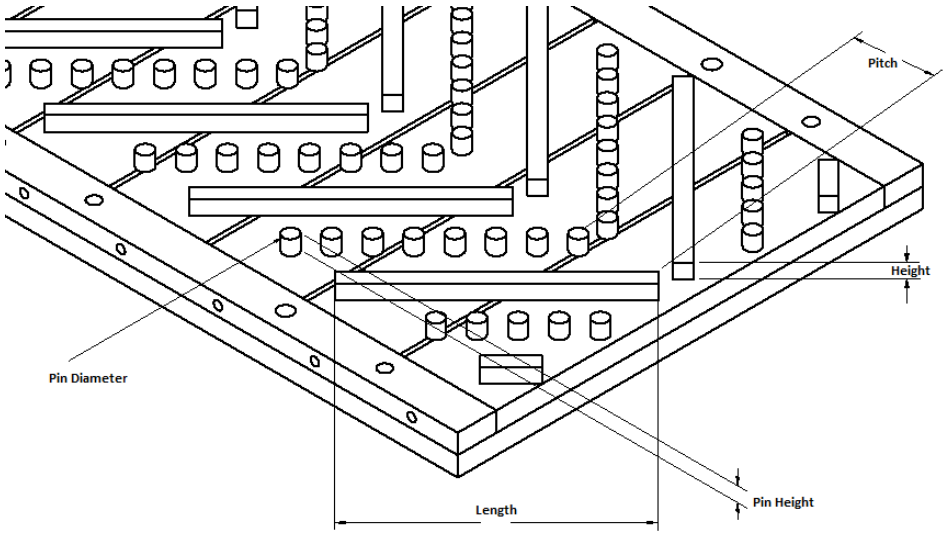

Figure 5 – Description of geometric specification. The P/e ratio is the pitch between a set of ribs/pins and the height refers to the height of the pin/rib. Modified from Rallabandi et al. [5].

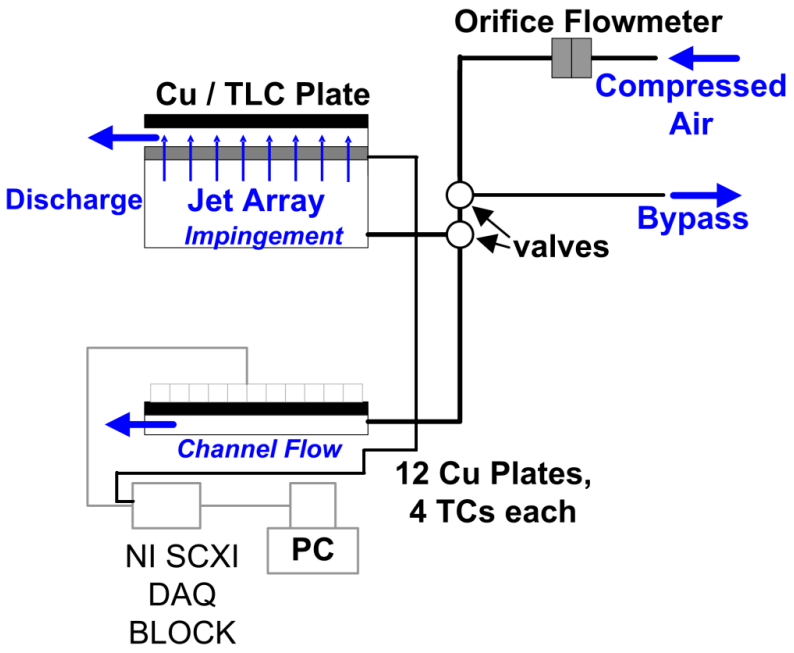

Figure 6 – Schematic of test section. Modified from Rallabandi et al. [5].

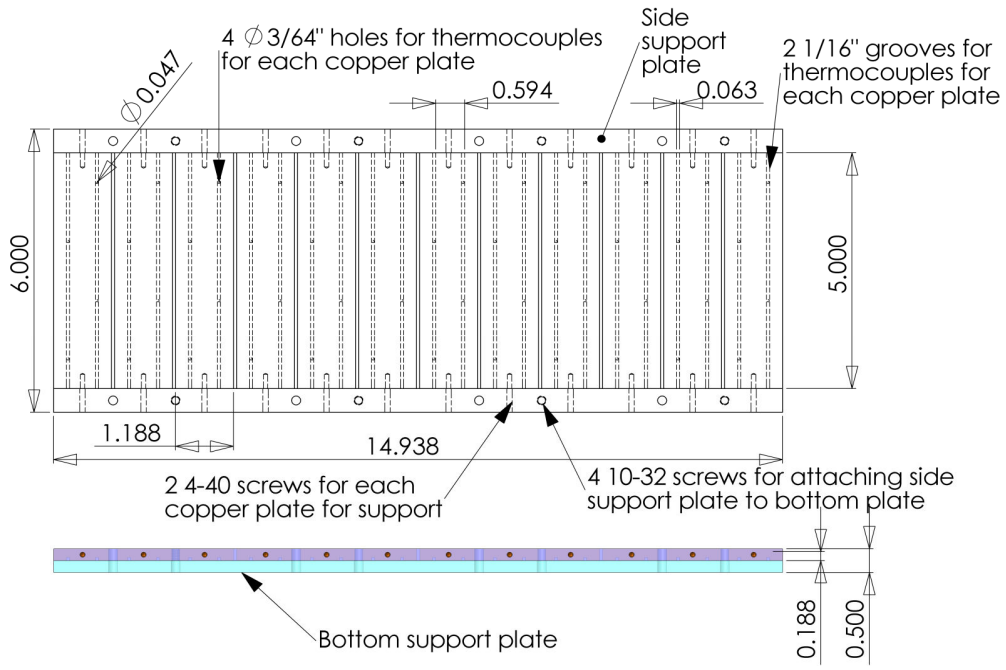

Figure 7 – Copper plate arrangement. Provided from Rallabandi et al. [5].

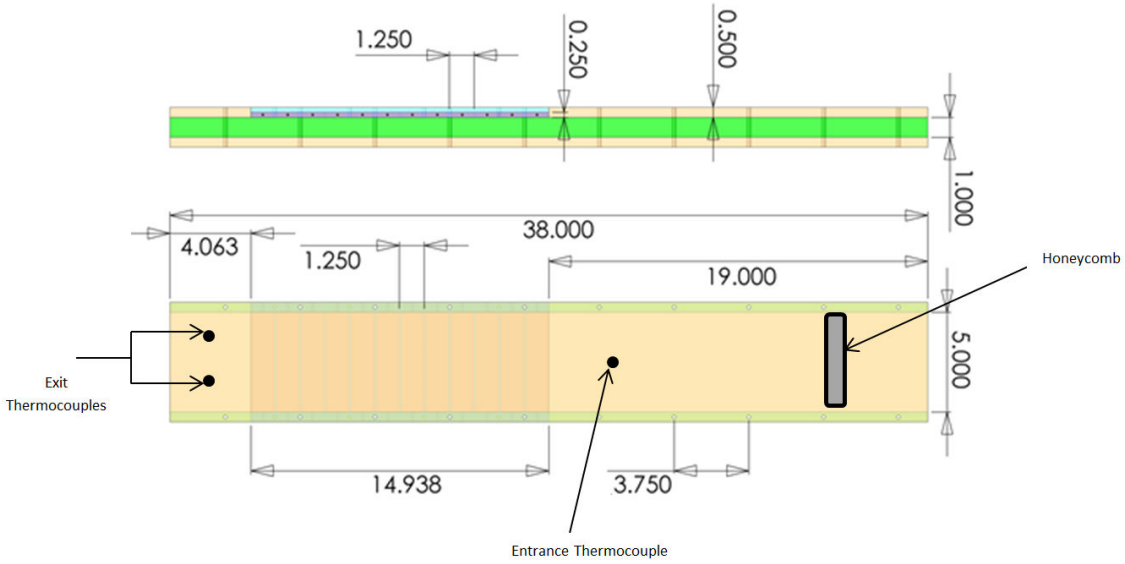

Figure 8 – Channel flow geometric specification. Provided from Rallabandi et al. [5].

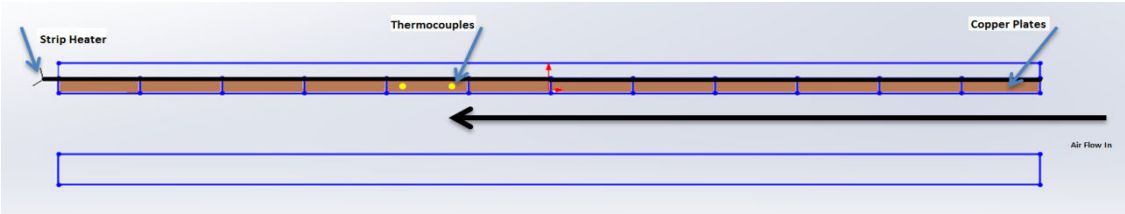

Figure 9 – Channel flow passage for the steady state heat transfer test.

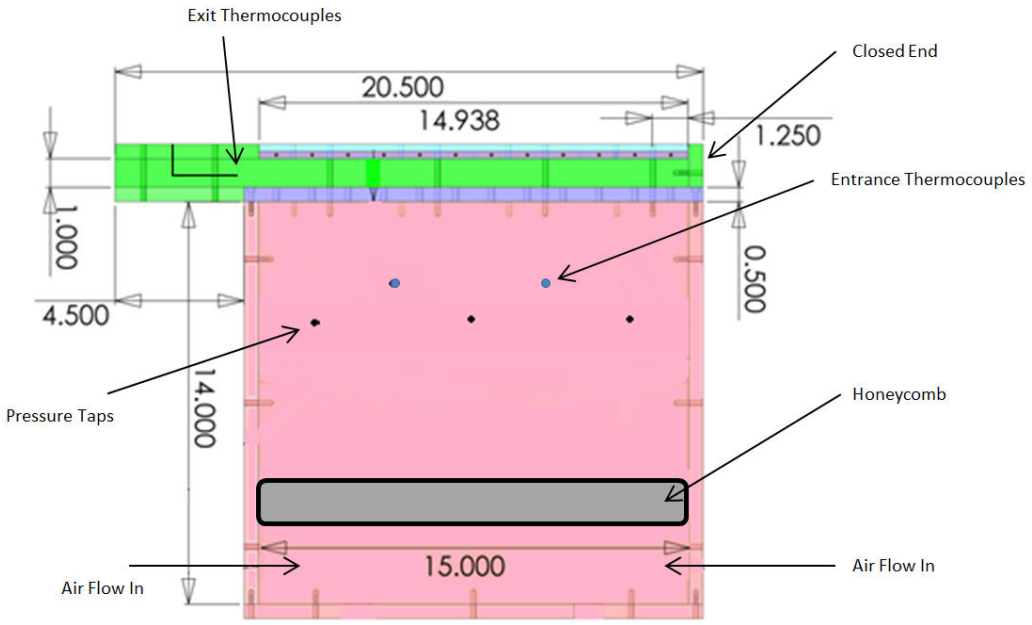

Figure 10 – Jet impingement geometric specification. Provided from Rallabandi et al. [9].

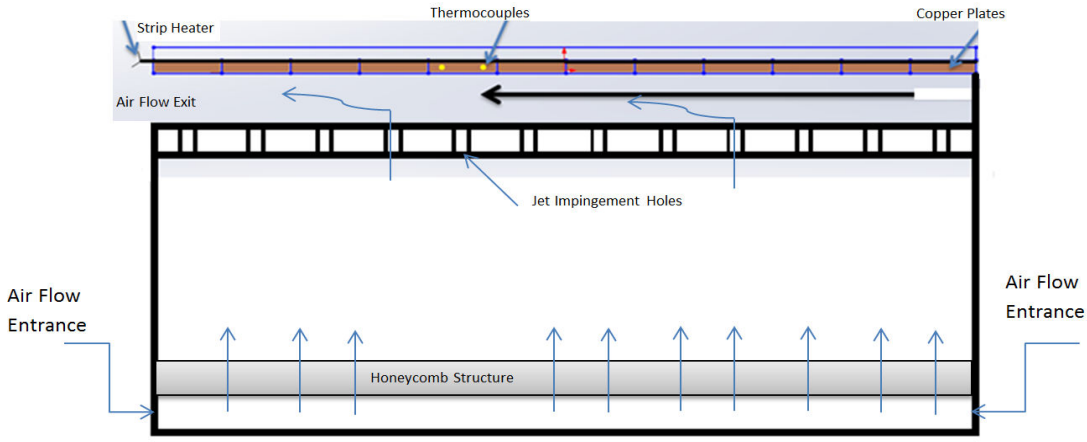

Figure 11 – Jet impingement configuration for the steady state heat transfer experiment.

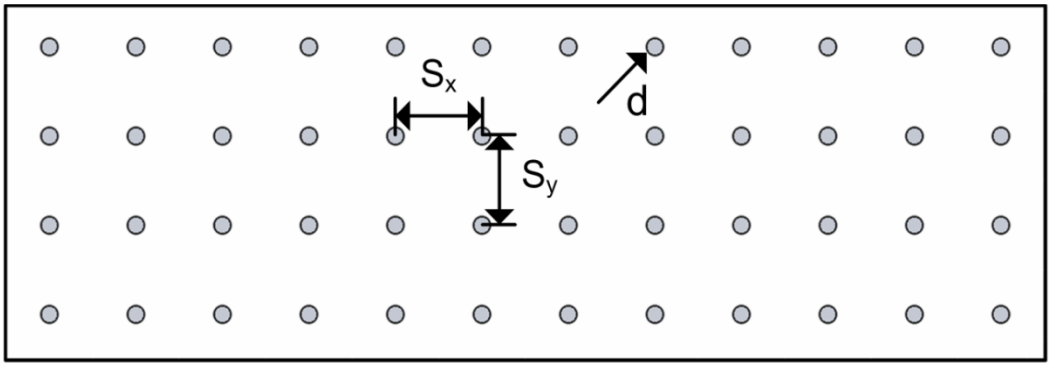

Figure 12 – Jet impingement hole arrangement. Diameter of jet hole = 0.25 in. Jet Spacing: S_x=1.25in S_y=1.25in. Provided from Rallabandi et.al [5].

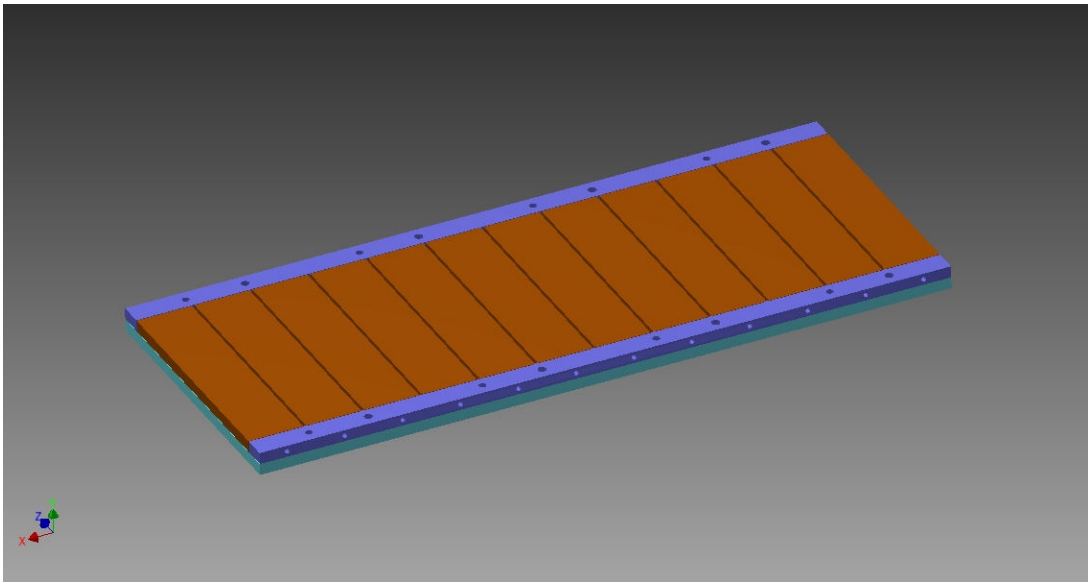

Figure 13 – Smooth copper plate arrangement. Provided from Rallabandi et al. [5].

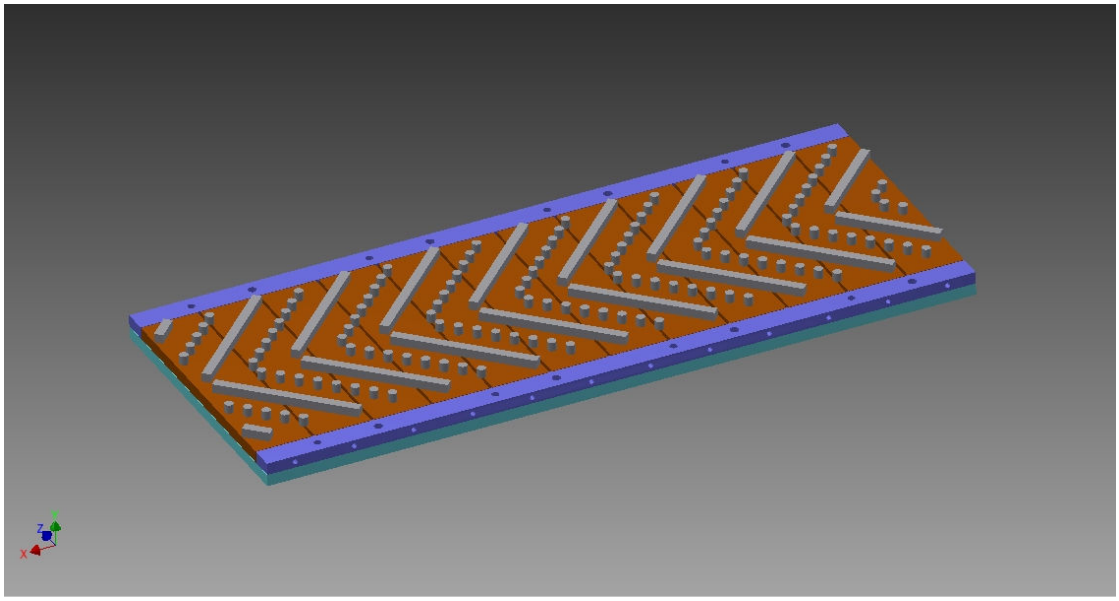

Figure 14 – Copper plates arrangement with ribs and pins P/e Ratio of 5. Modified from Rallabandi et al. [5].

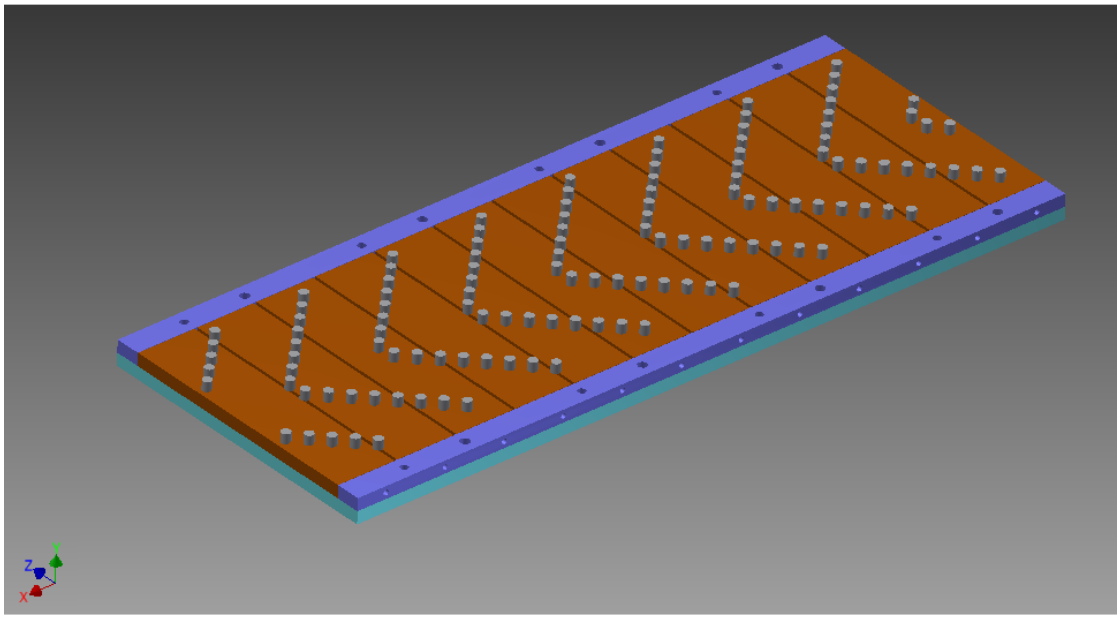

Figure 15 – Copper plates arrangement with all pins P/e ratio of 10. Modified from Rallabandi et al. [5].

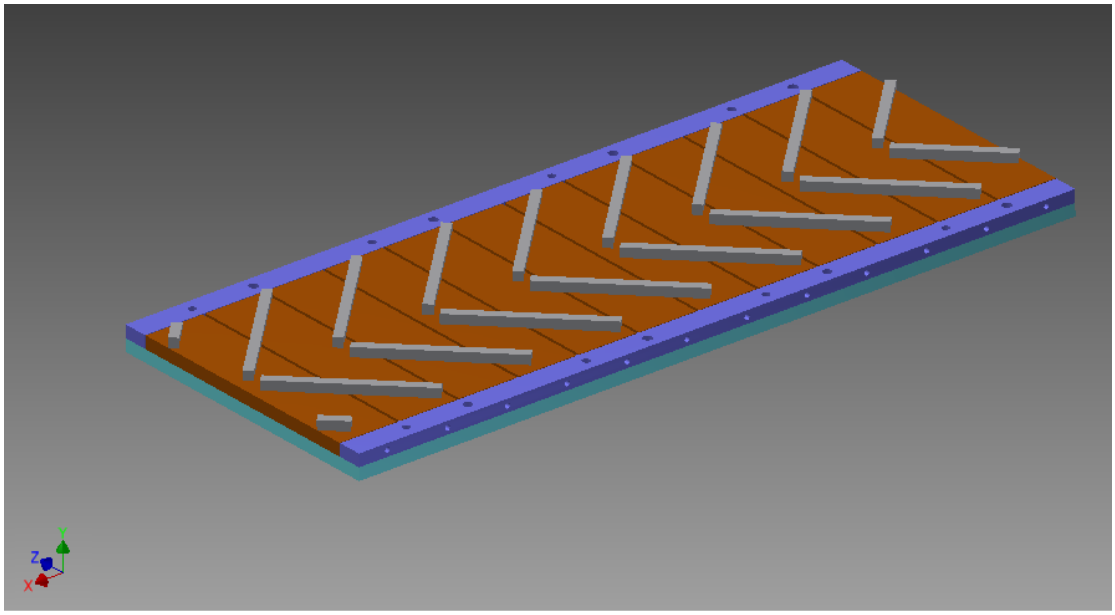

Figure 16 – Copper plates arrangement with all ribs P/e ratio of 10. Modified from Rallabandi et al. [5].

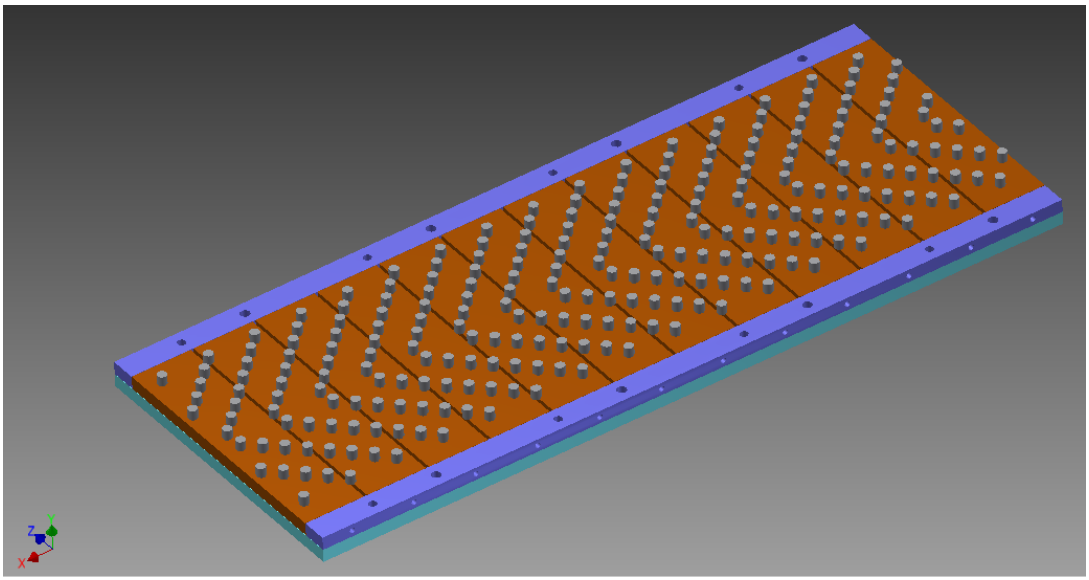

Figure 17 – Copper plates arrangement with all pins P/e ratio of 5. Modified from Rallabandi et al. [5].

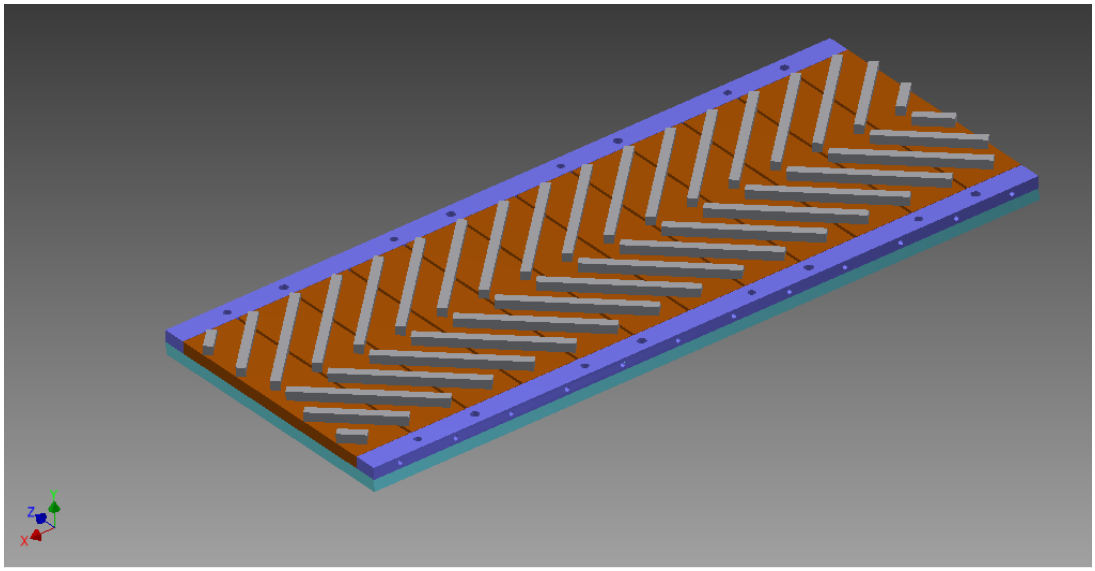

Figure 18 – Copper plates arrangement with all ribs P/e Ratio of 5. Modified from Rallabandi et al. [5].

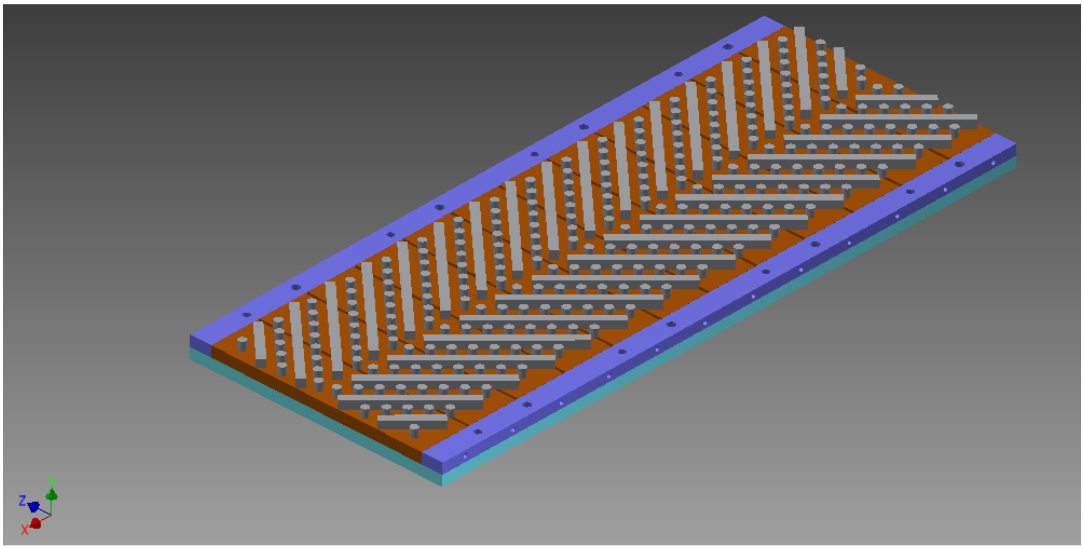

Figure 19 – Copper plates arrangement with ribs and pins P/e ratio of 2.5. Modified from Rallabandi et al. [5].

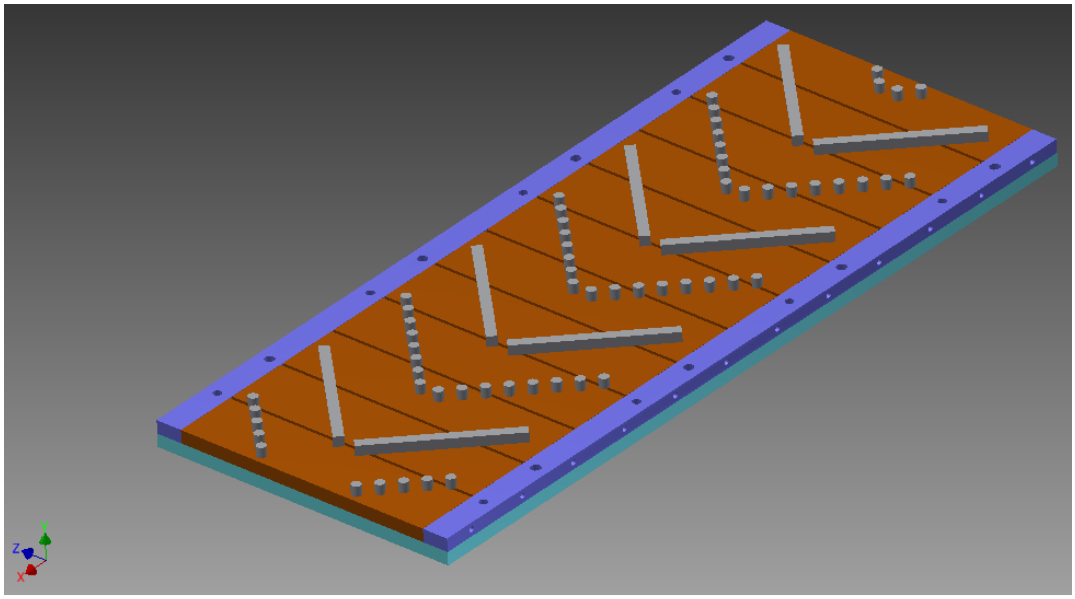

Figure 20 – Copper plates arrangement with ribs and pins P/e ratio of 10. Modified from Rallabandi et al. [5].

Table 5 – Experimental instrumentation

Instrument Type	Model Number	Quantity
Copper Pins D = 0.0048m, H = 0.0048m	-	252
Copper Rib L=0.0749m, W=0.0048m, H=0.0048m	-	28
Copper Rib L=0.0537m, W=0.0048m, H=0.0048m	-	2
Copper Rib L=0.0224m, W=0.0048m, H=0.0048m	-	2
Copper Rib L=0.048m, W=0.0048m, H=0.0048m	-	2
Copper Rib L=0.0143m, W=0.0048m, H=0.0048m	-	2
Copper Plates, L=0.0316, W=0.127m	-	12
OMEGA T-Type Thermocouples	TT-T-36-SLE	61
DWYER Incline Manometer	424	2
FLUKE Digital Multimeter	25	1
Staco Variac	-	1
Marsh Pressure Gage	-	1
Boston Bosflex Tubing 1”	-	20ft
South Bay Plastic Tubing (1000ft)	Y-105	1
WATLOW Silicone Heater	D50149500	1
National Instruments 32 Channel Isothermal Terminal Block	SCXI 1303	2
National Instruments DAQ	SCXI 1000	1
LOCTITE Instant Adhesive Super Bounder	415	2
GE Waterproof Silicone	-	1
FOAMULAR Insulation	-	2
Davey Air Compressor	08-2001685	1
Apollo 1” Ball Valves	500 WCG	2
1.5” Orifice Plate	-	1
LABVIEW (Sofware)	-	1
Microsoft Office	-	1

Table 6 - Heat loss correlations. Provided by Rallabandi et al. (5)

$\dot{Q}_{Loss}$ [W/m^2]	
Plate Number	**Correlation**
1	4.971*(T_w-T_room) -3.165
2	4.619*(T_w-T_room) - 3.1885
3	4.4005*(T_w-T_room) - 4.4468
4	4.2822*(T_w-T_room) - 4.1835
5	4.2167*(T_w-T_room) - 4.1028
6	4.1822*(T_w-T_room) - 4.535
7	4.2188*(T_w-T_room) - 3.0621
8	4.302*(T_w-T_room) - 2.6274
9	4.4677*(T_w-T_room) - 5.4158
10	4.7165*(T_w-T_room) - 4.7162
11	5.1098*(T_w-T_room) - 5.062
12	4.5246*(T_w-T-room) - 4.152

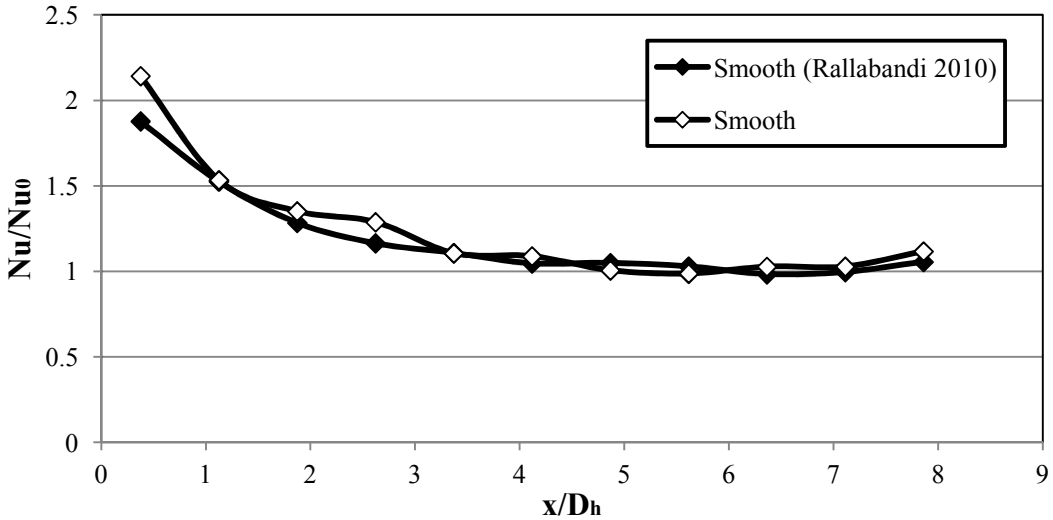

Figure 21 – Comparison of Nusselt number ratios for the smooth case at Re=10K of the current data and previous data for channel flow.

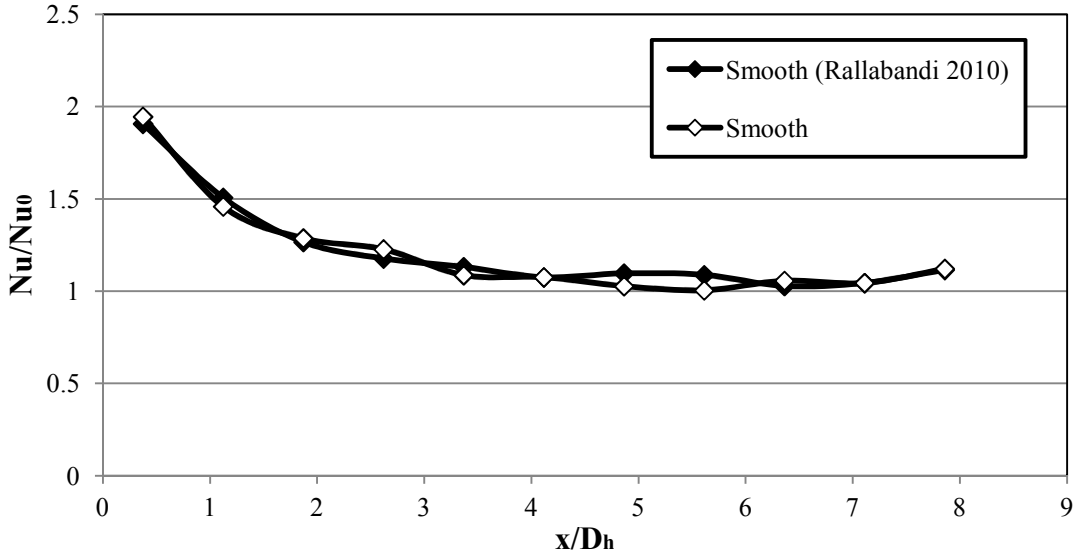

Figure 22 – Comparison of Nusselt number ratios for the smooth case at Re=20K of the current data and previous data for channel flow.

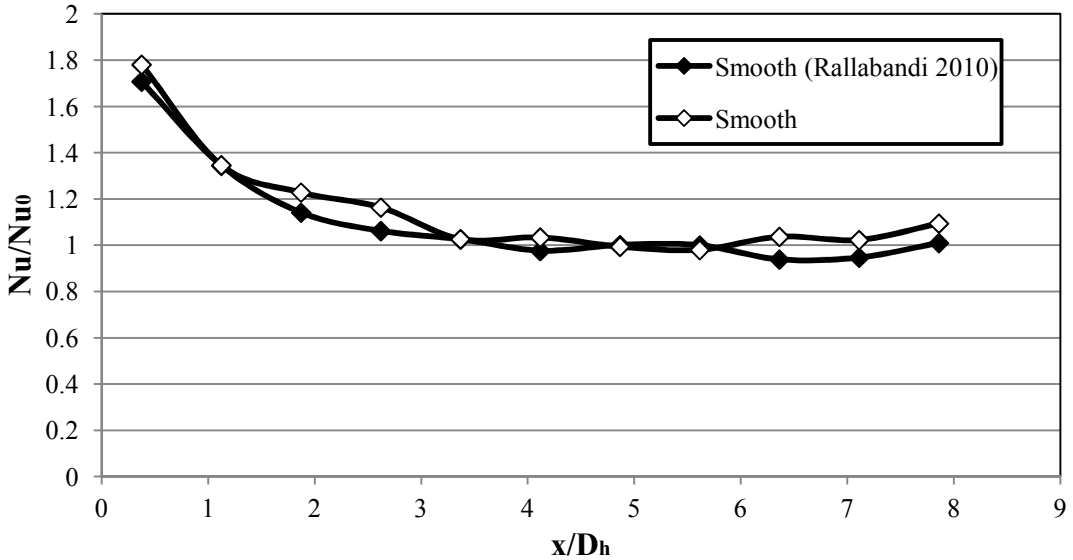

Figure 23 – Comparison of Nusselt number ratios for the smooth case at Re=30K of the current data and previous data for channel flow.

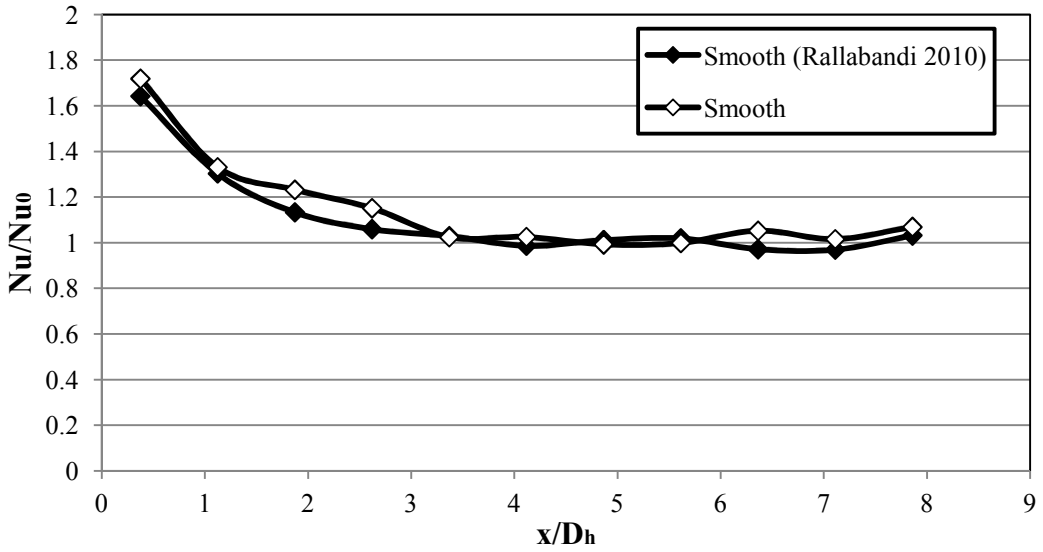

Figure 24 – Comparison of Nusselt number ratios for the smooth case at Re=40K of the current data and previous data for channel flow.

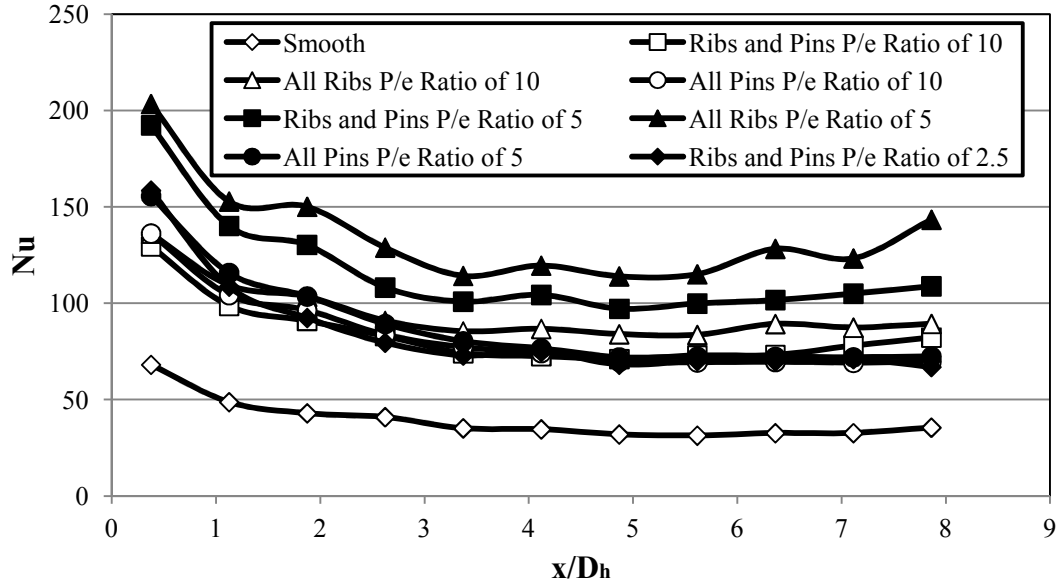

Figure 25 – Nusselt number comparison for channel flow at Re=10K.

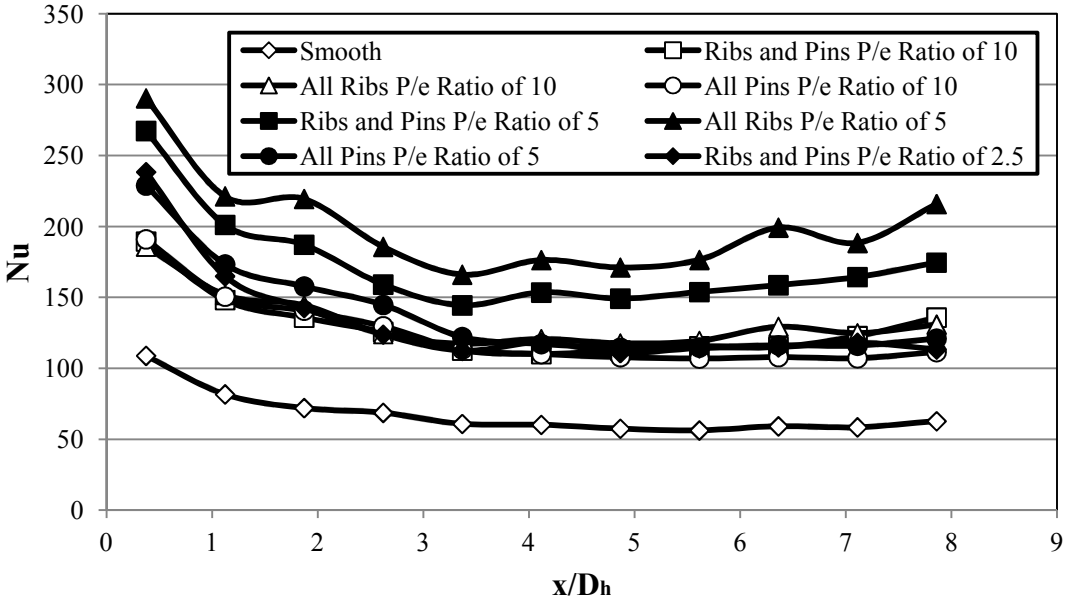

Figure 26 – Nusselt number comparison for channel flow at Re=20K.

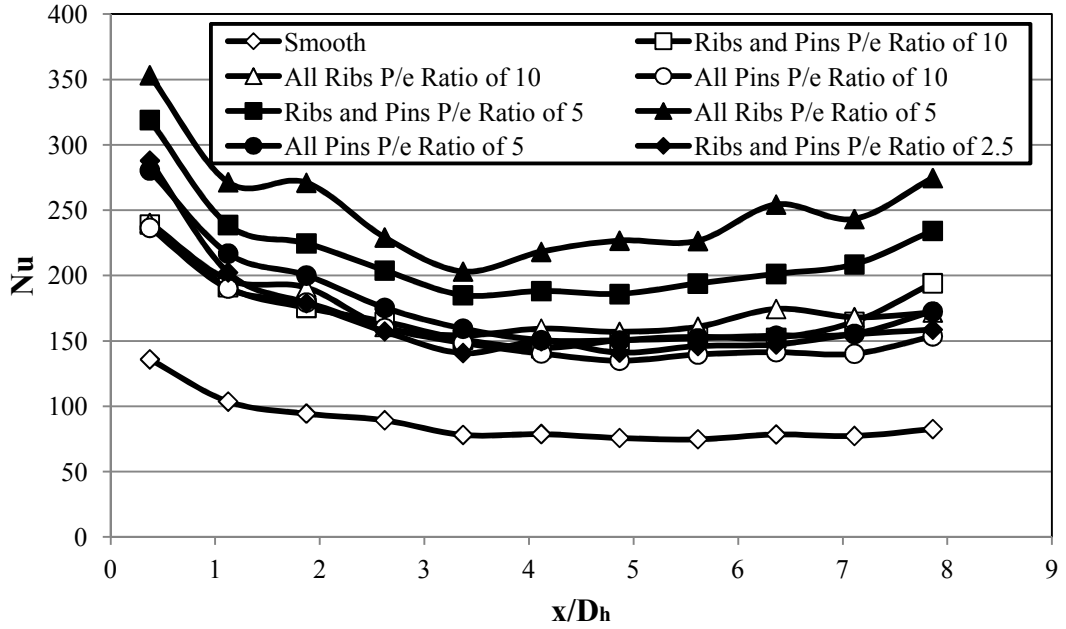

Figure 27 – Nusselt number comparison for channel flow at Re=30K.

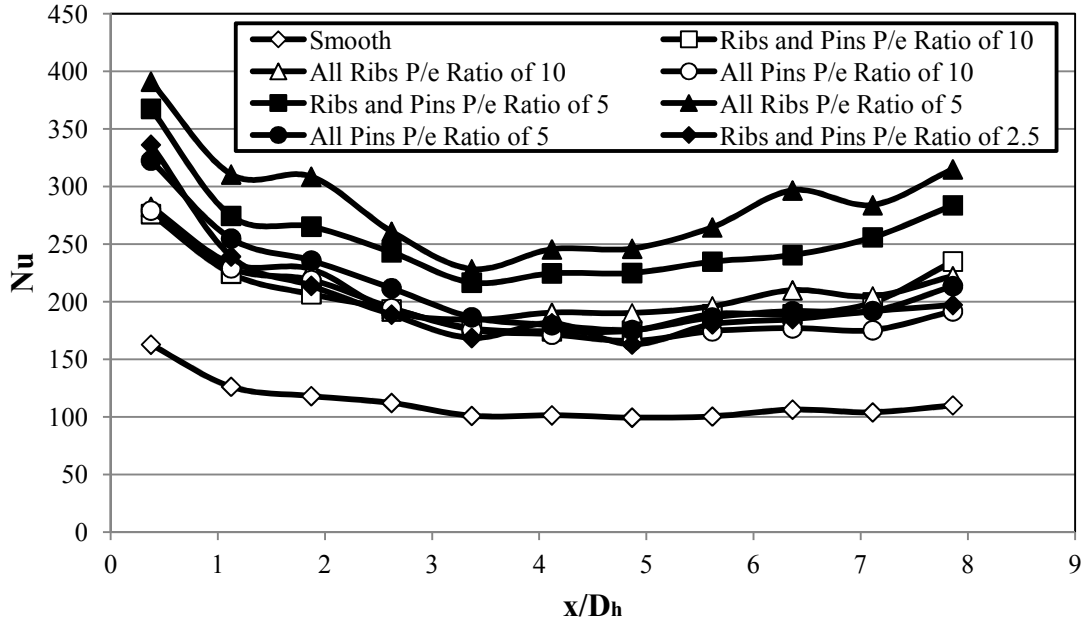

Figure 28 – Nusselt number comparison for channel flow at Re = 40K.

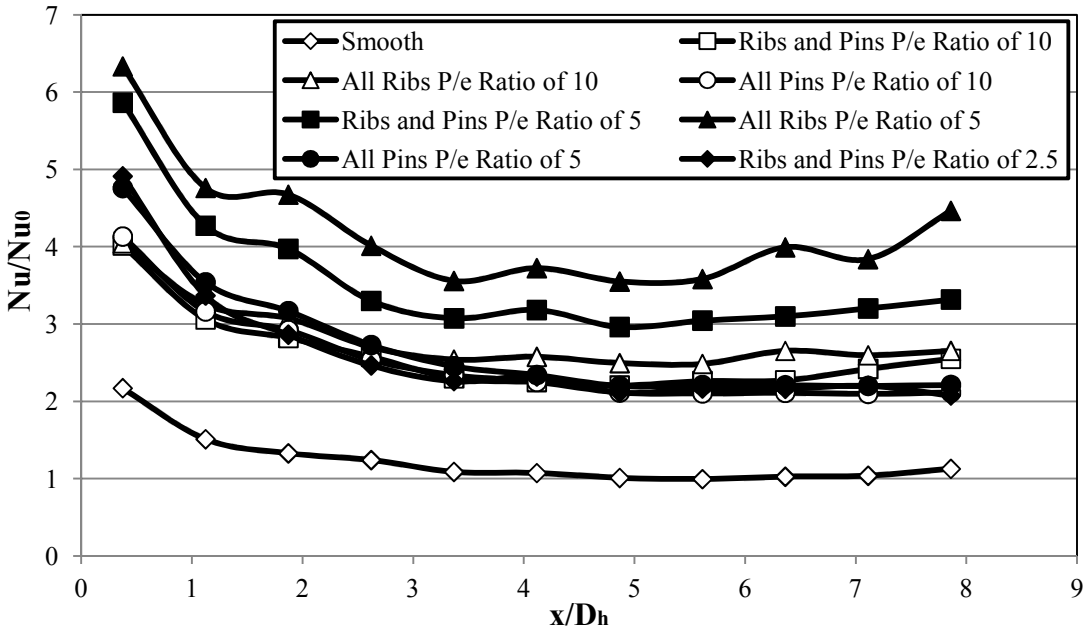

Figure 29 – Nusselt number ratio comparison for channel flow at Re=10K.

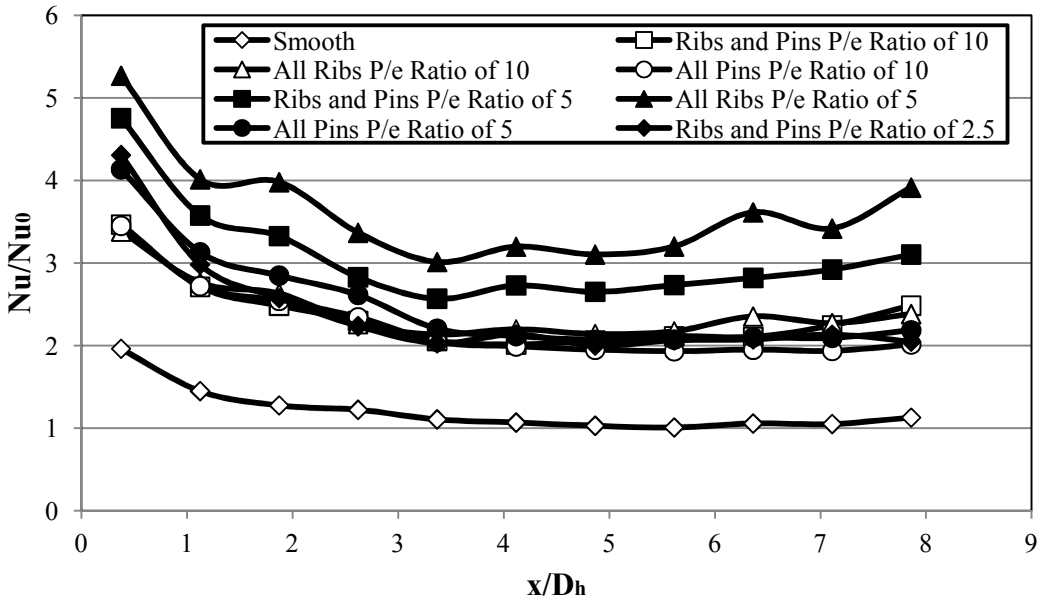

Figure 30 – Nusselt number ratio comparison for channel flow at Re=20K.

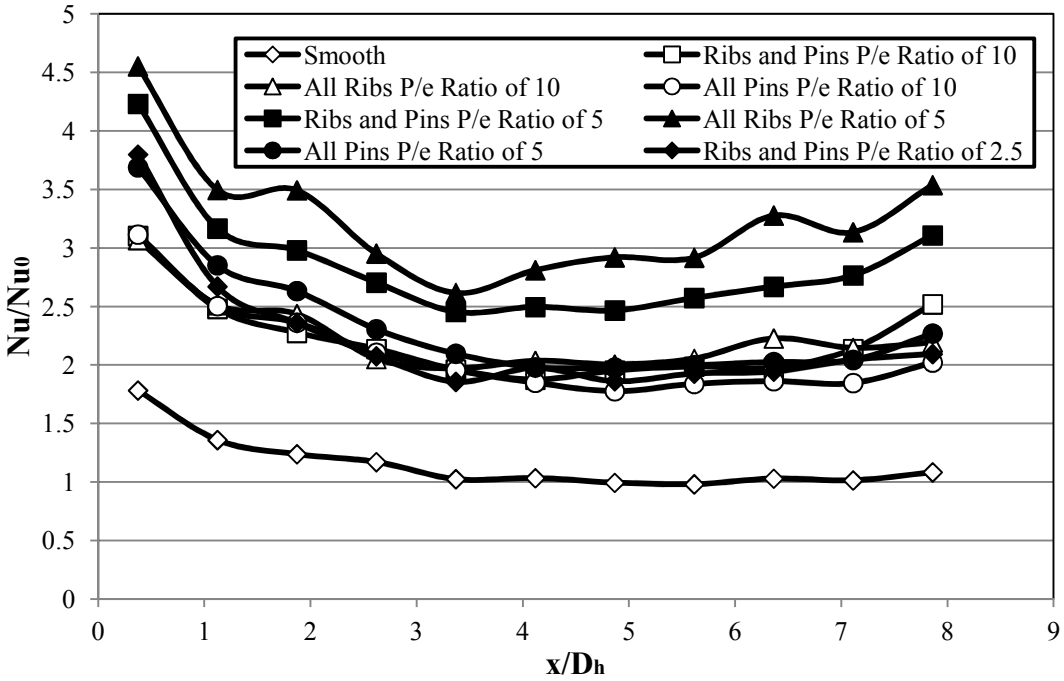

Figure 31 – Nusselt number ratio comparison for channel flow at Re=30K.

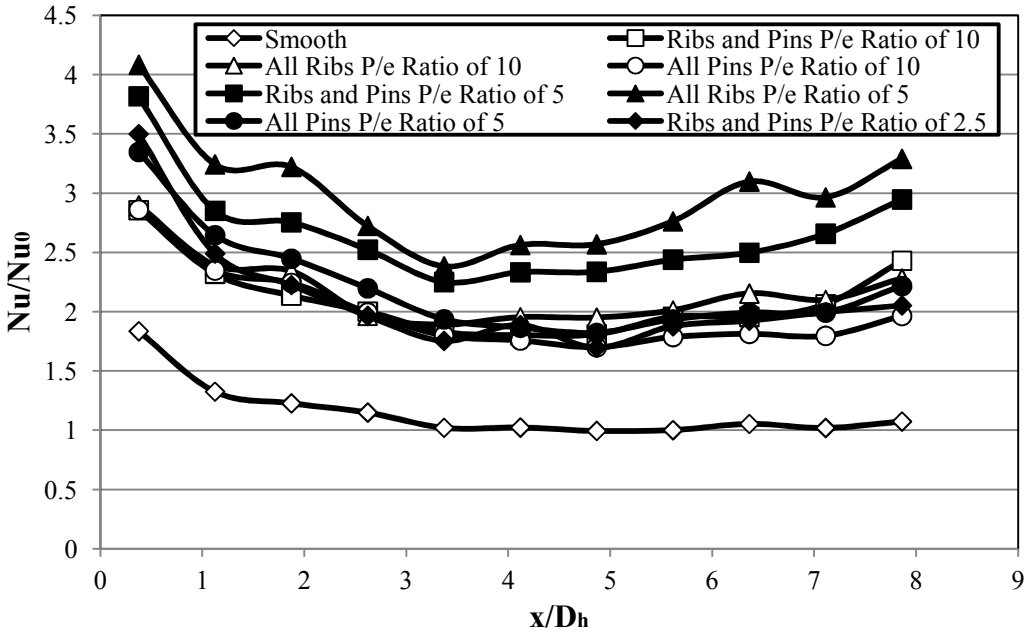

Figure 32 – Nusselt number ratio comparison for channel flow at Re=40K.

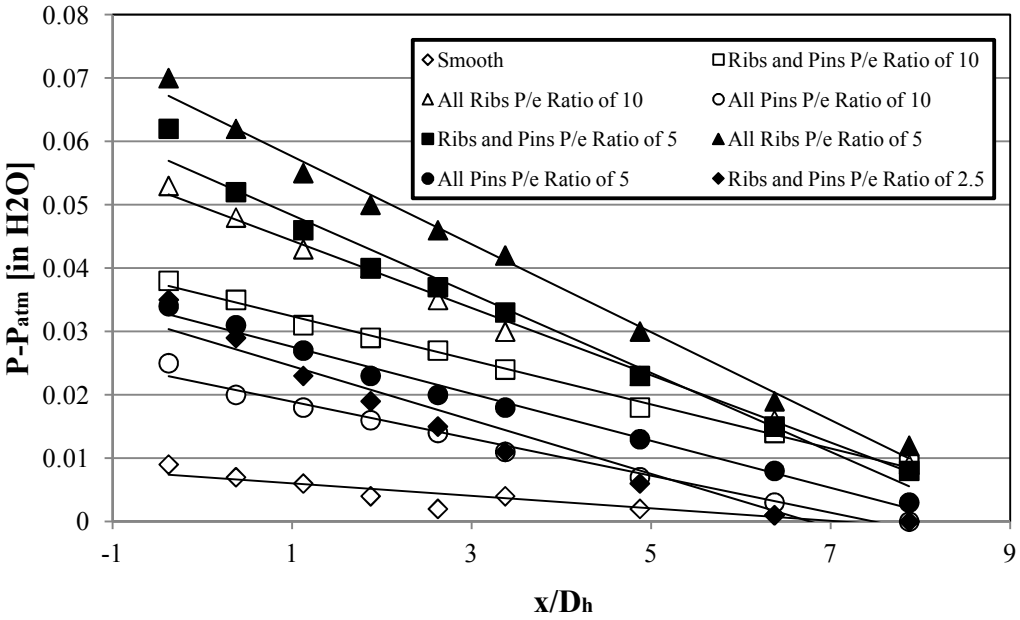

Figure 33 - Pressure drop across channel for Re=10K.

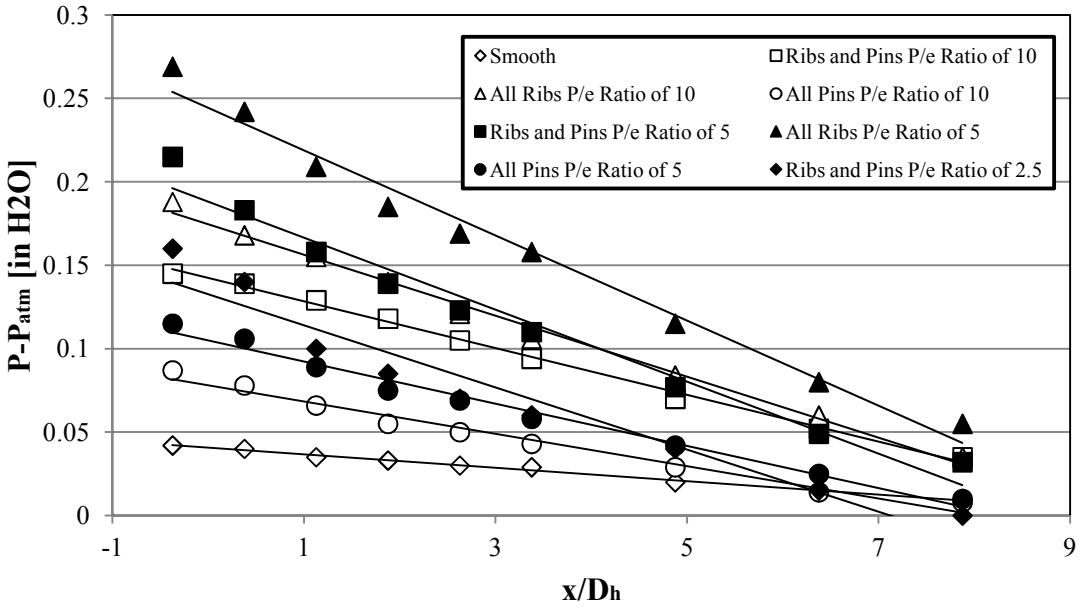

Figure 34 - Pressure drop across channel for Re=20K.

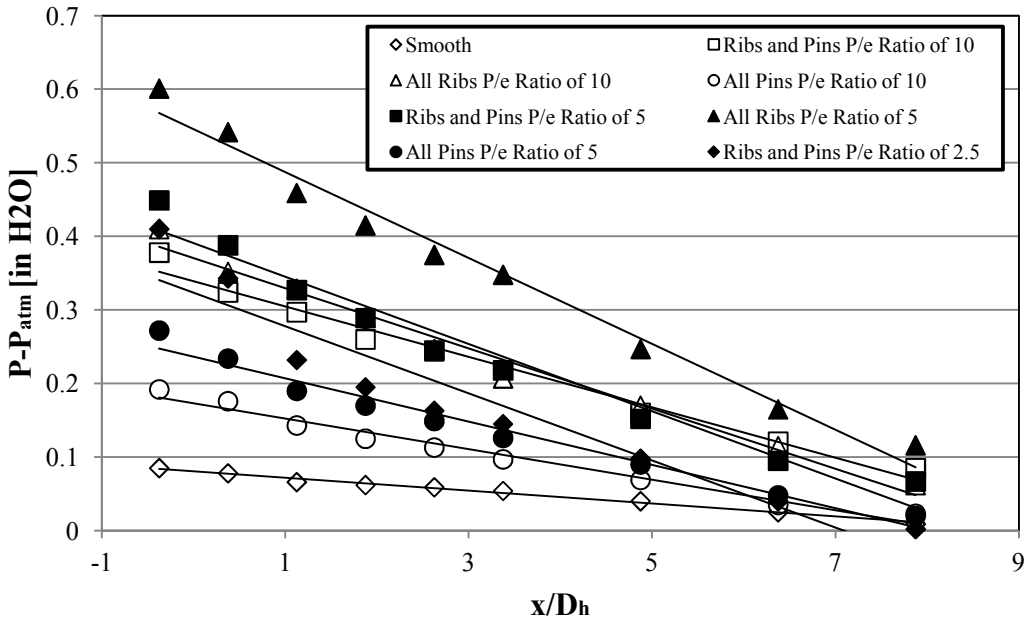

Figure 35 - Pressure drop across channel for Re=30K.

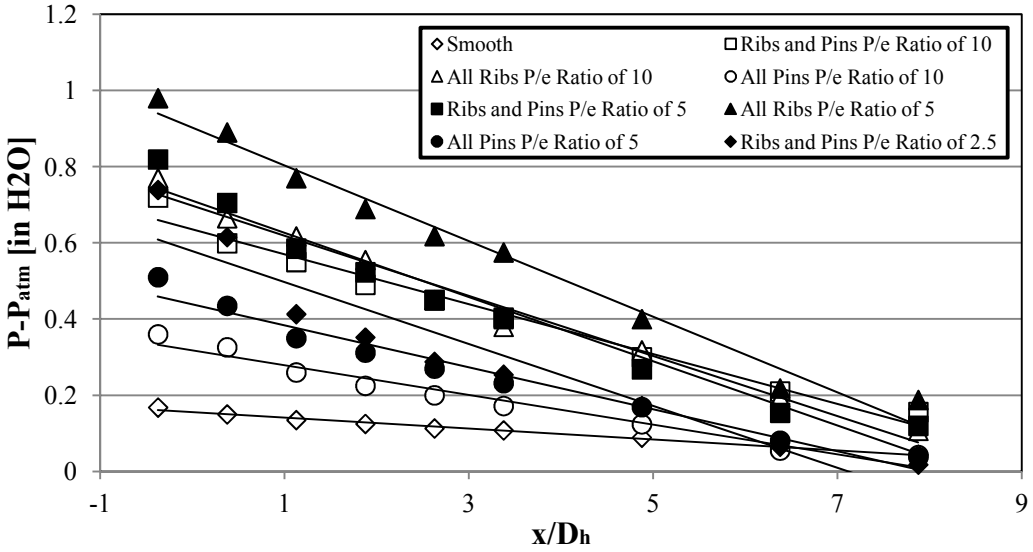

Figure 36 - Pressure drop across channel for Re=40K.

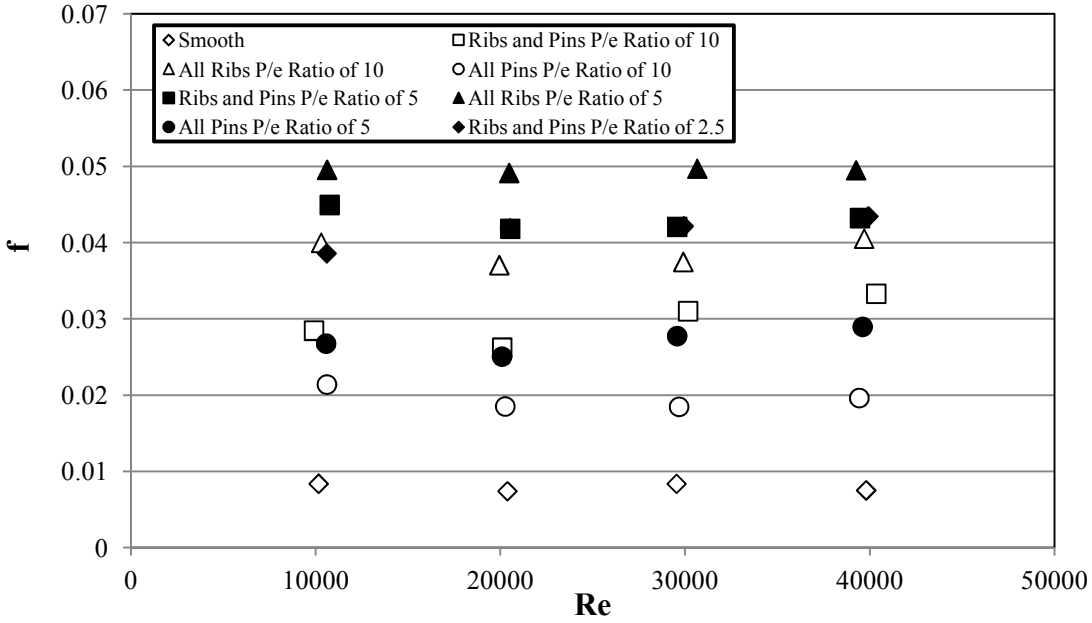

Figure 37 – Friction factor for channel flow cases.

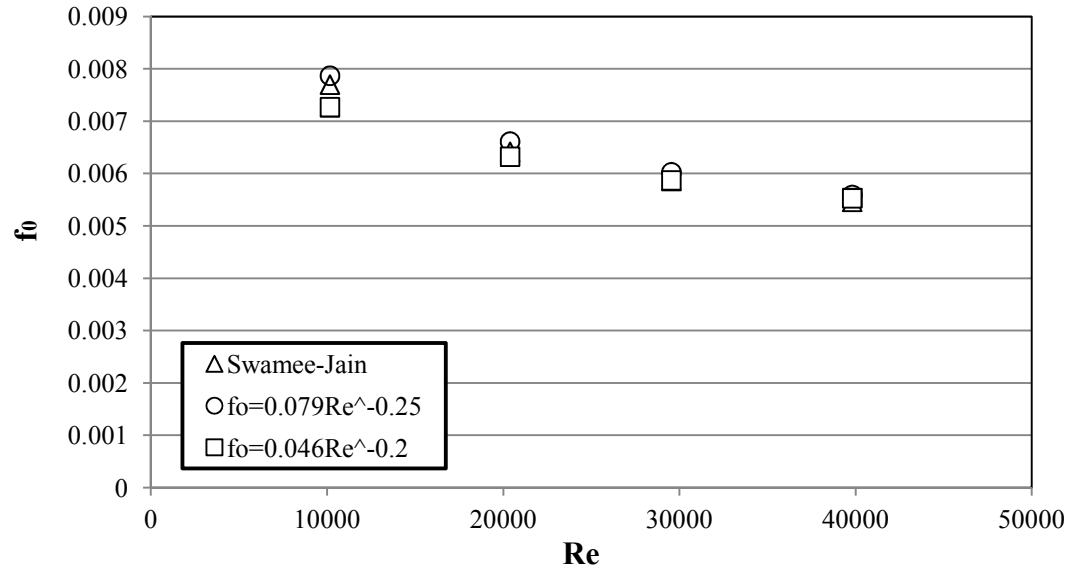

Figure 38 – Smooth friction factor relations comparison.

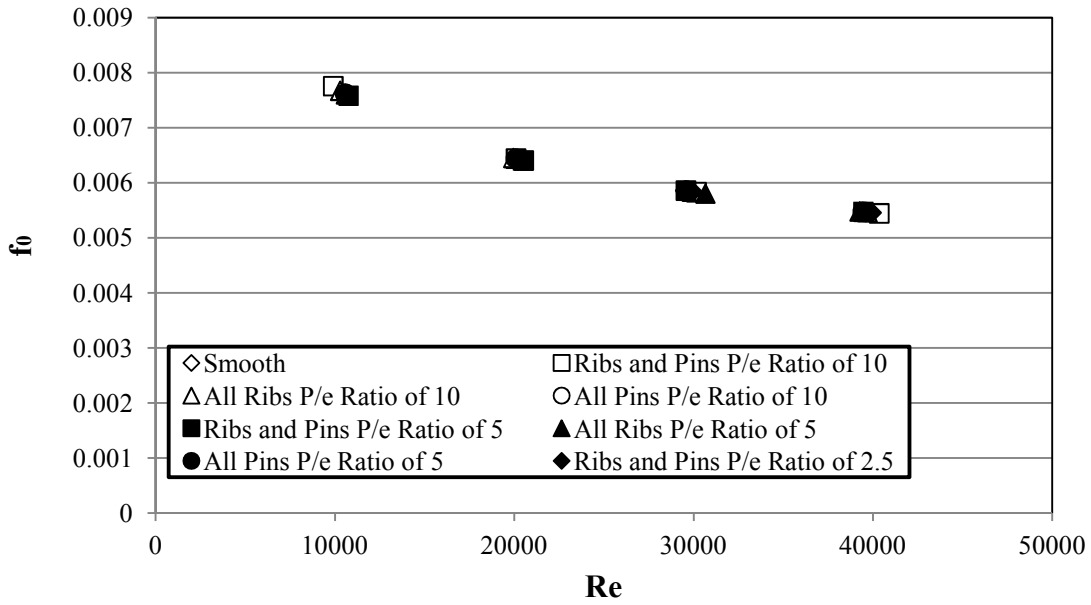

Figure 39 – Empirical friction factor for channel flow cases.

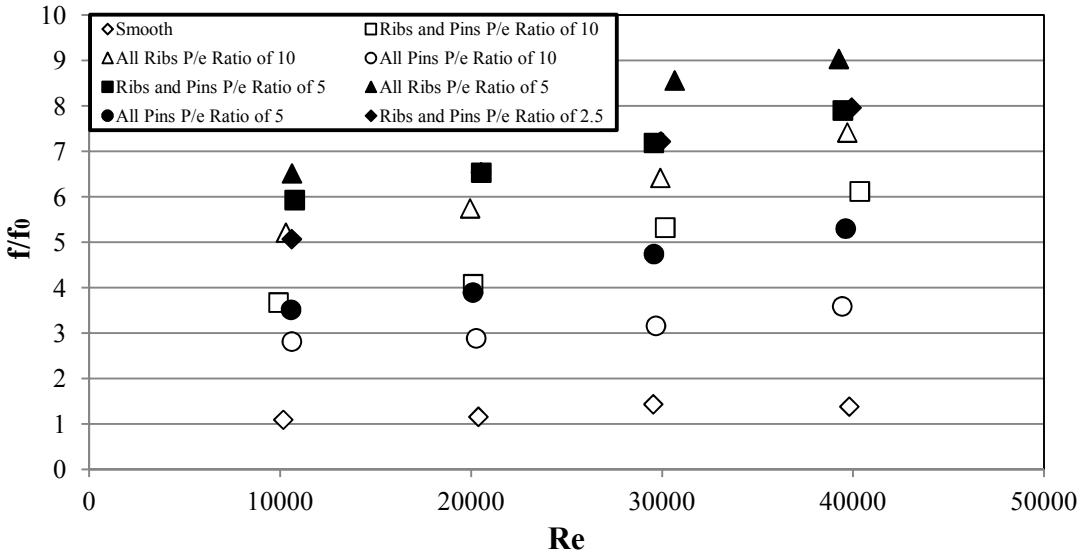

Figure 40 – Friction factor ratio for channel flow experiment.

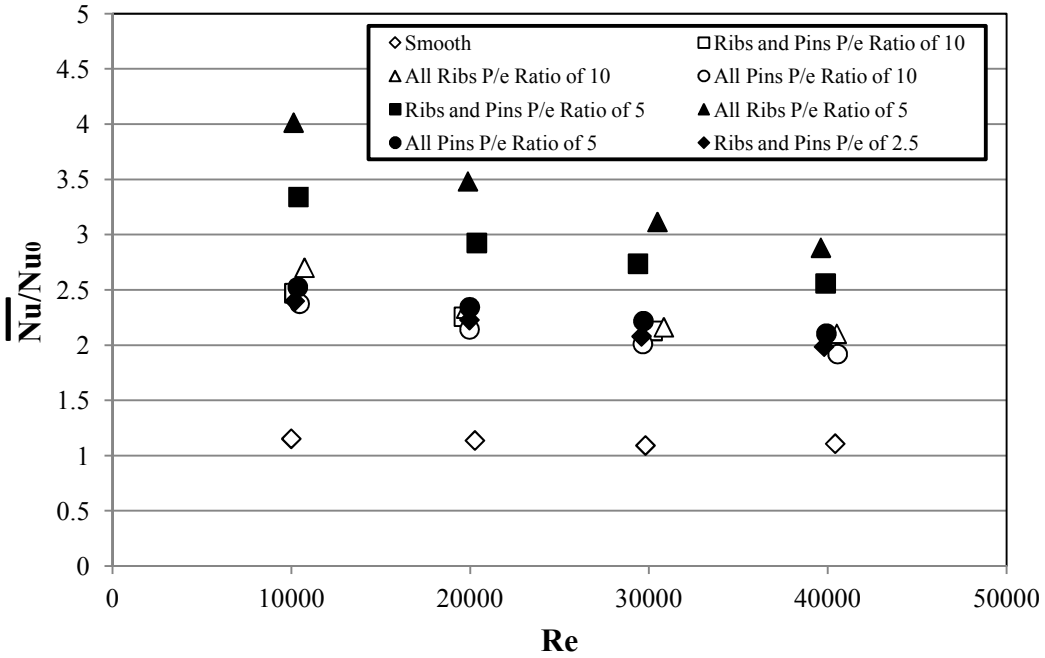

Figure 41 – Average Nusselt number ratio for channel flow experiment.

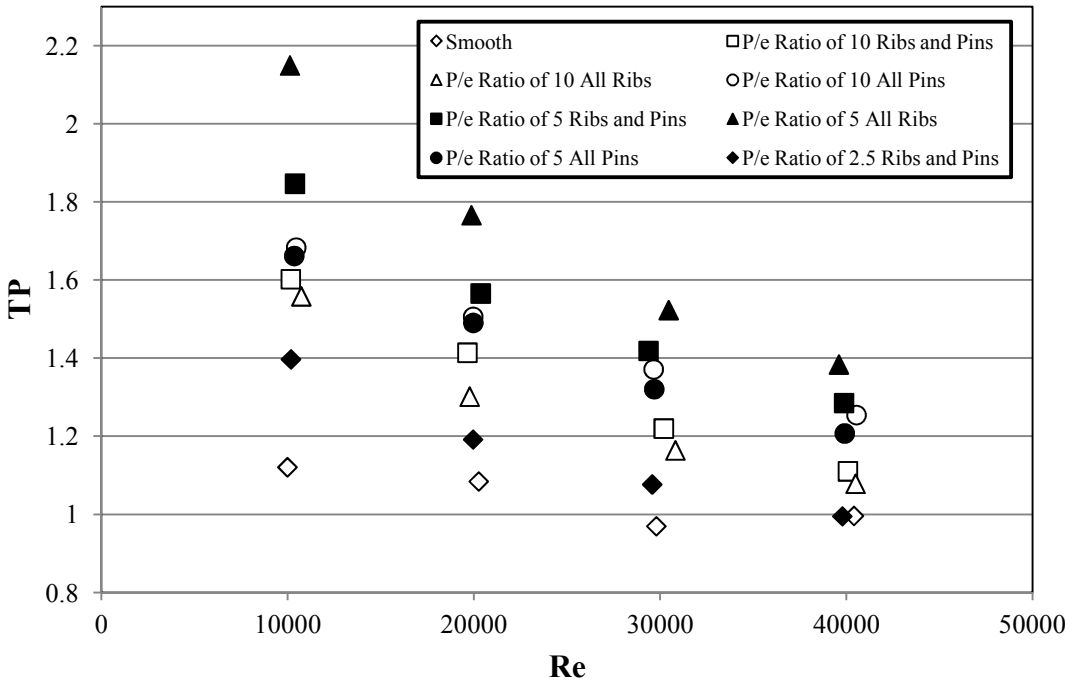

Figure 42 – Thermal performance results for channel flow experiment.

Table 7 – Percent area increase for different rough surface configurations.

	Total Surface Area (in^2)	**Total Surface Area (m^2)**	**Percent Area Increase of Rib Turbulators**	**Percent Area Increase of Pin Fins**	**Surface Area Percent Increase**
Smooth	74.7	0.0482	0%	0%	0%
All Ribs P/e Ratio of 10	93.46	0.0603	100%	0%	25.11%
All Ribs P/e Ratio of 5	112.3	0.0724	100%	0%	50.33%
Ribs and Pins P/e Ratio of 10	90.960	0.0587	57.89%	42.11%	21.77%
Ribs and Pins P/e Ratio of 5	107.38	0.0693	57.41%	42.59%	43.75%
Ribs and Pins P/e Ratio of 2.5	140.13	0.0904	57.46%	42.54%	87.59%
All Pins P/e Ratio of 10	88.62	0.0571	0%	100%	18.63%
All Pins P/e Ratio of 5	102.5	0.0662	0%	100%	37.22%

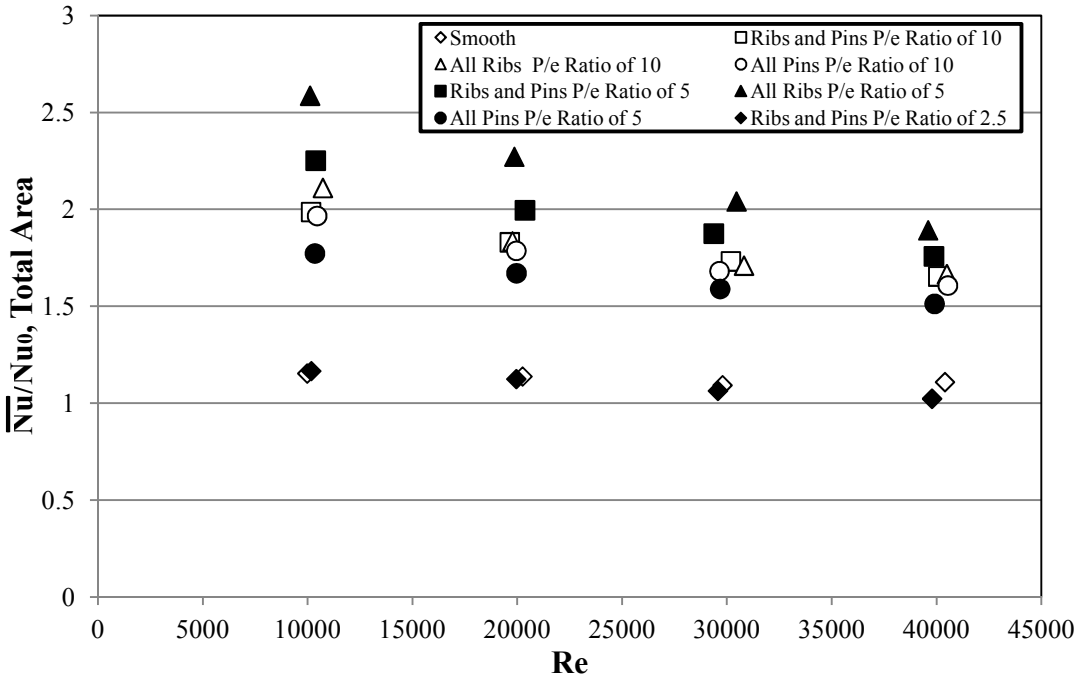

Figure 43 – Average Nusselt number ratio based off of total area.

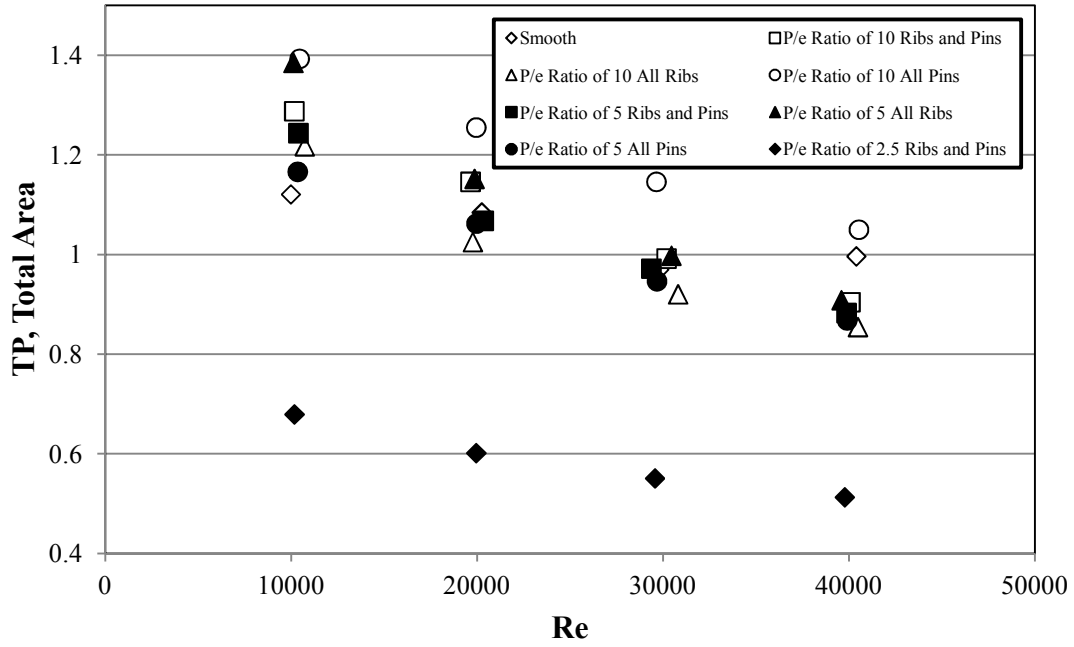

Figure 44 – Thermal performance results for channel flow based off of total area.

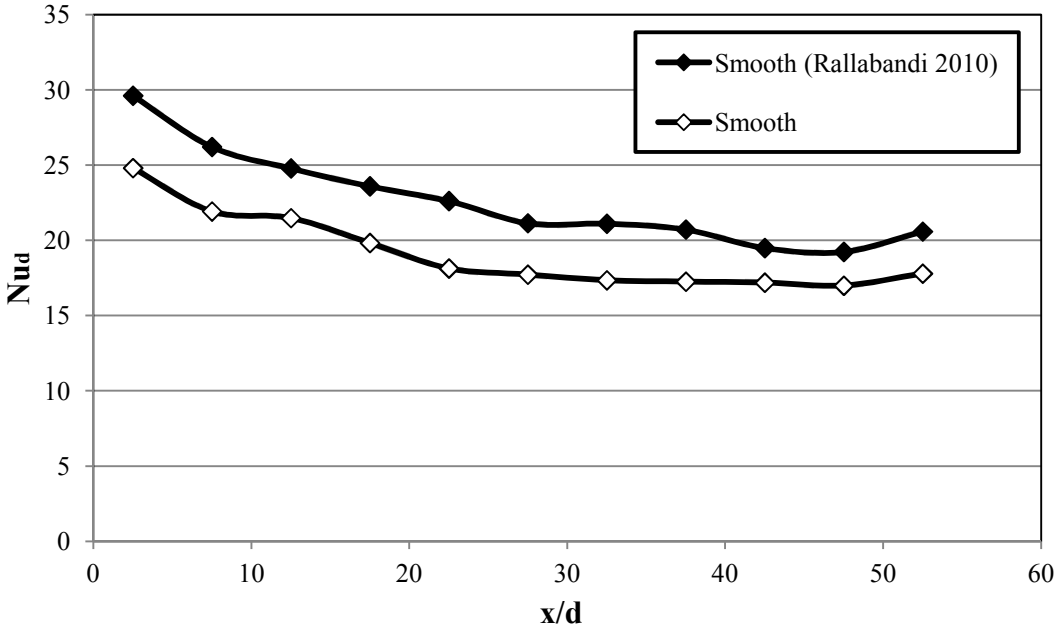

Figure 45 – Comparison of Nusselt number for the smooth case at Re=5K of the current data and previous data for jet impingement.

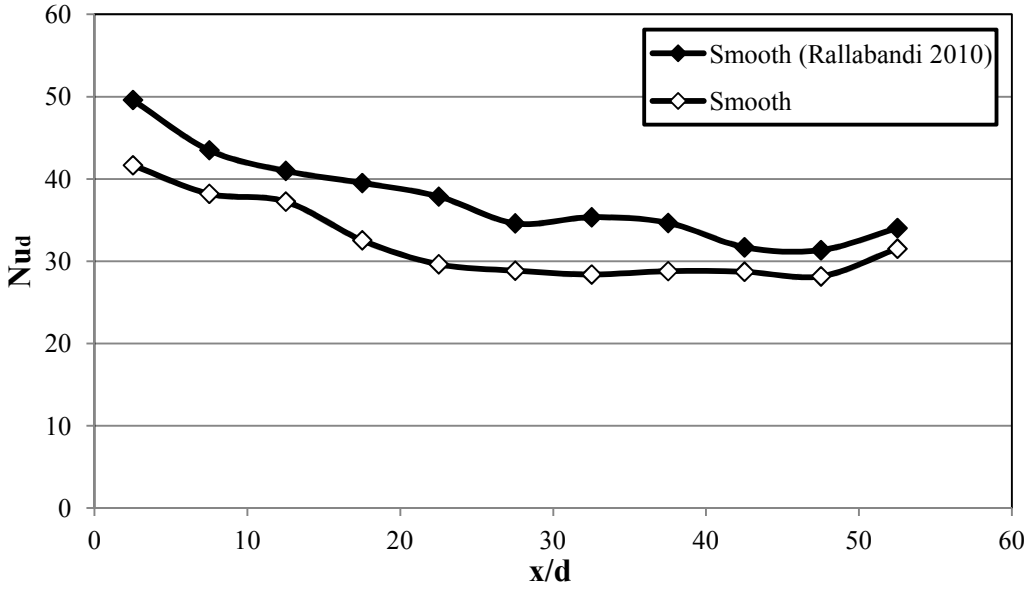

Figure 46 – Comparison of Nusselt number for the smooth case at Re=10K of the current data and previous data for jet impingement.

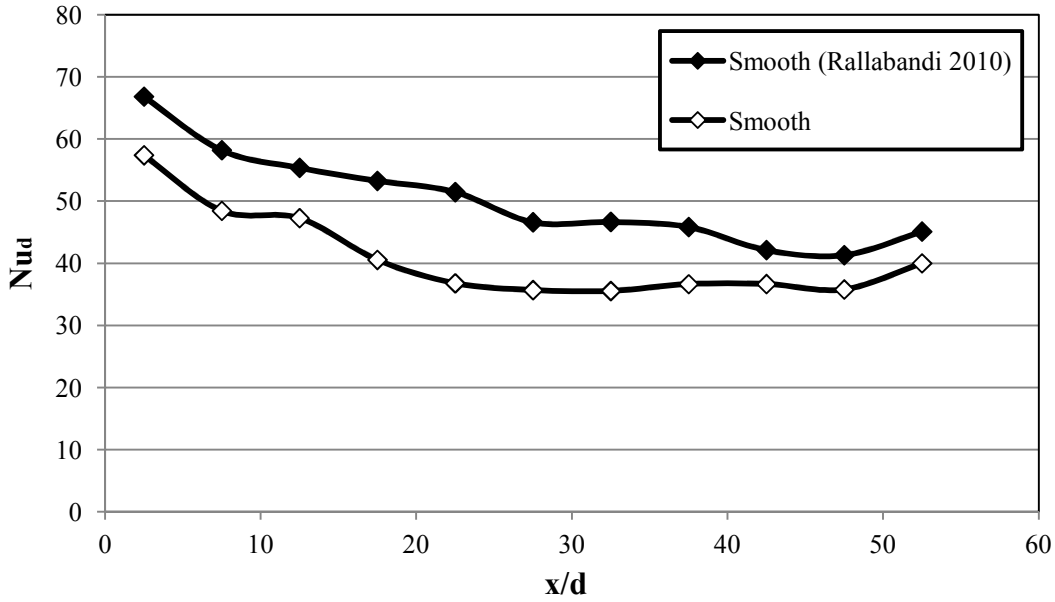

Figure 47 – Comparison of Nusselt number for the smooth case at Re=15K of the current data and previous data for jet impingement.

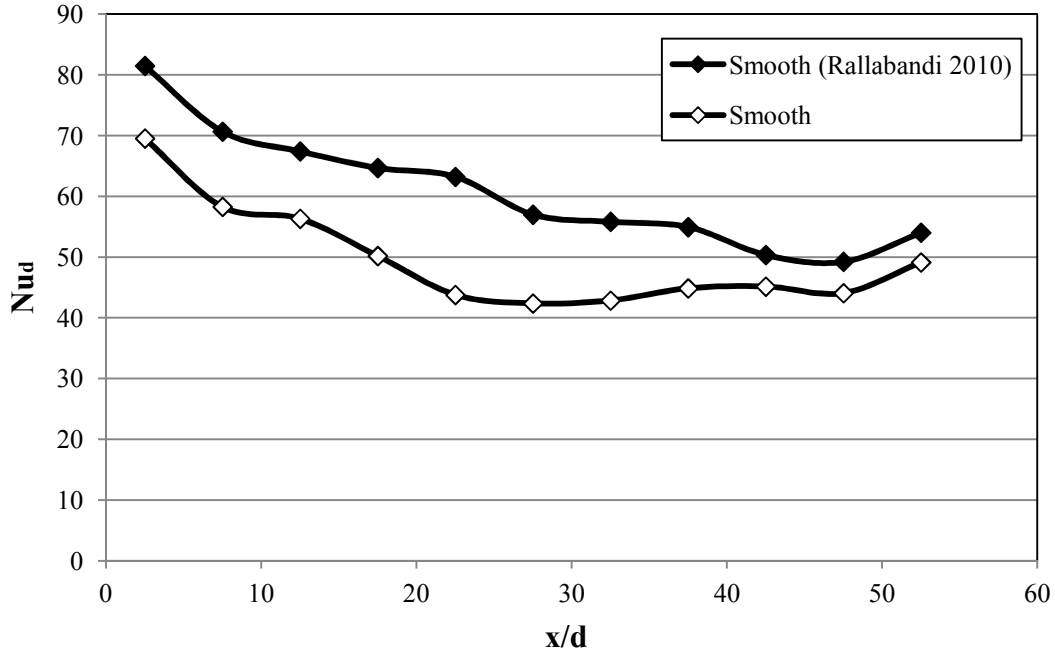

Figure 48 – Comparison of Nusselt number for the smooth case at Re=20K of the current data and previous data for jet impingement.

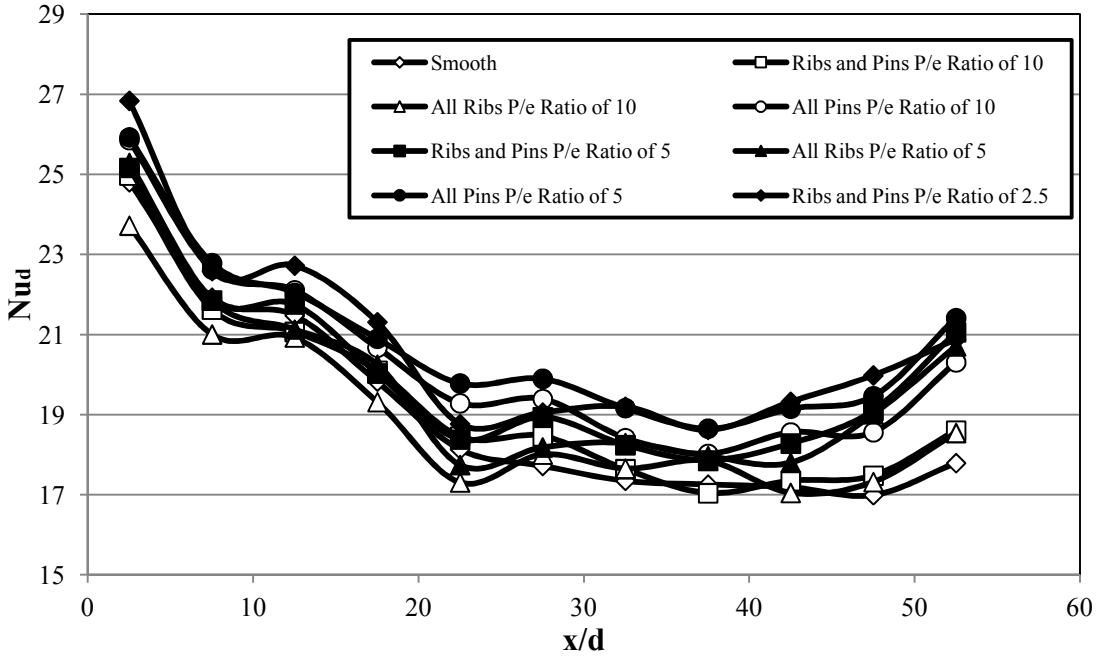

Figure 49 - Nusselt number comparison for jet impingement at Re=5K.

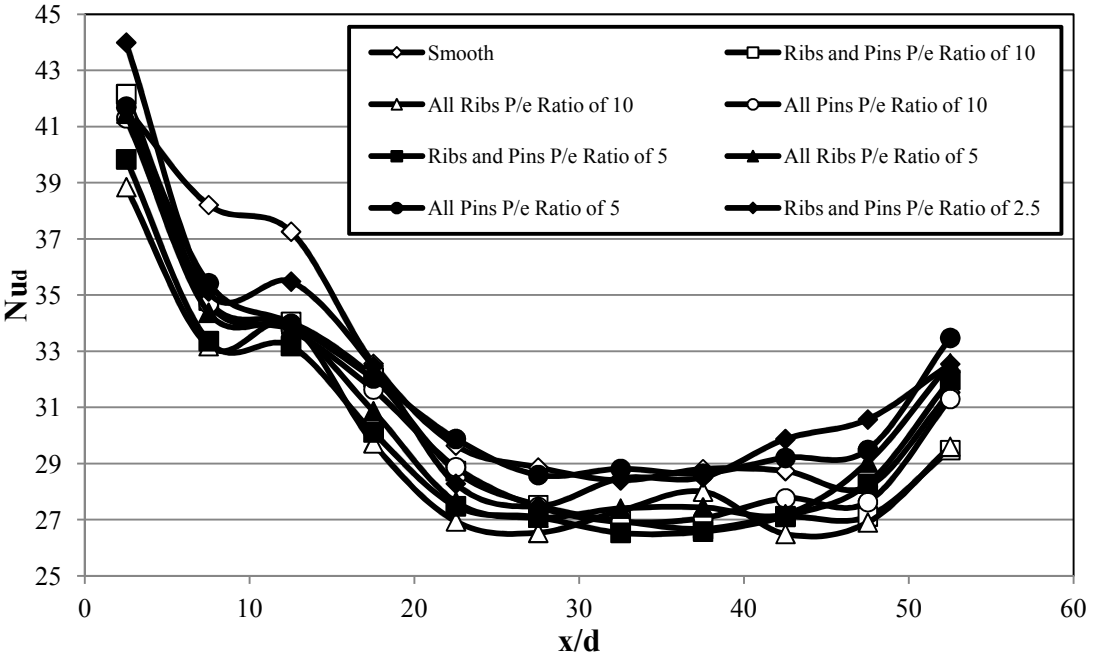

Figure 50 - Nusselt number comparison for jet impingement at Re=10K.

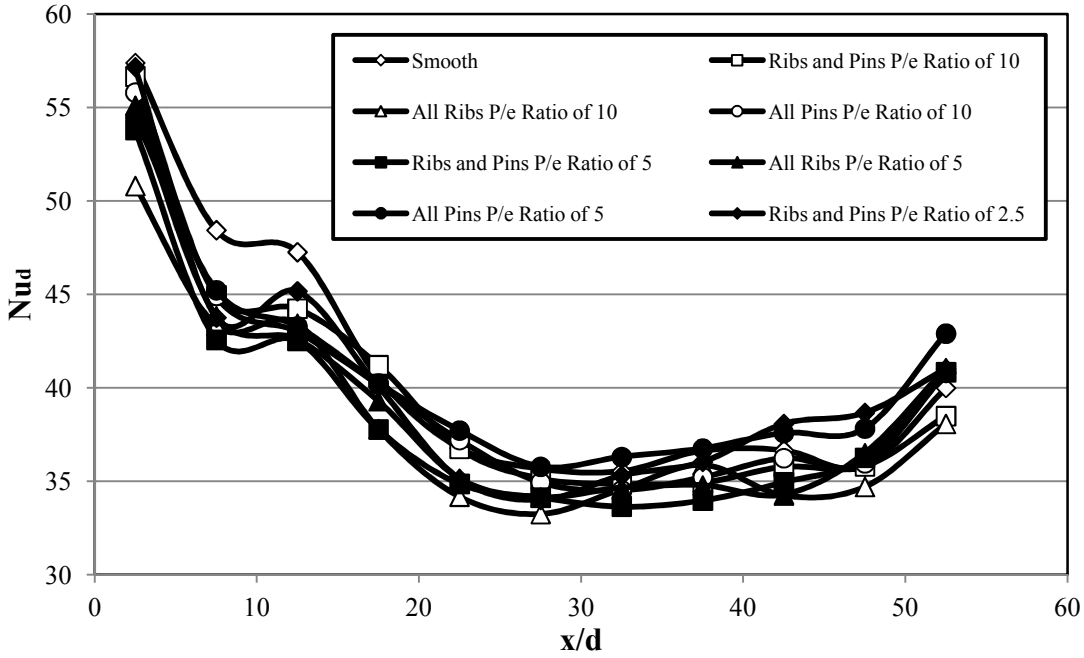

Figure 51 - Nusselt number comparison for jet impingement at Re=15K.

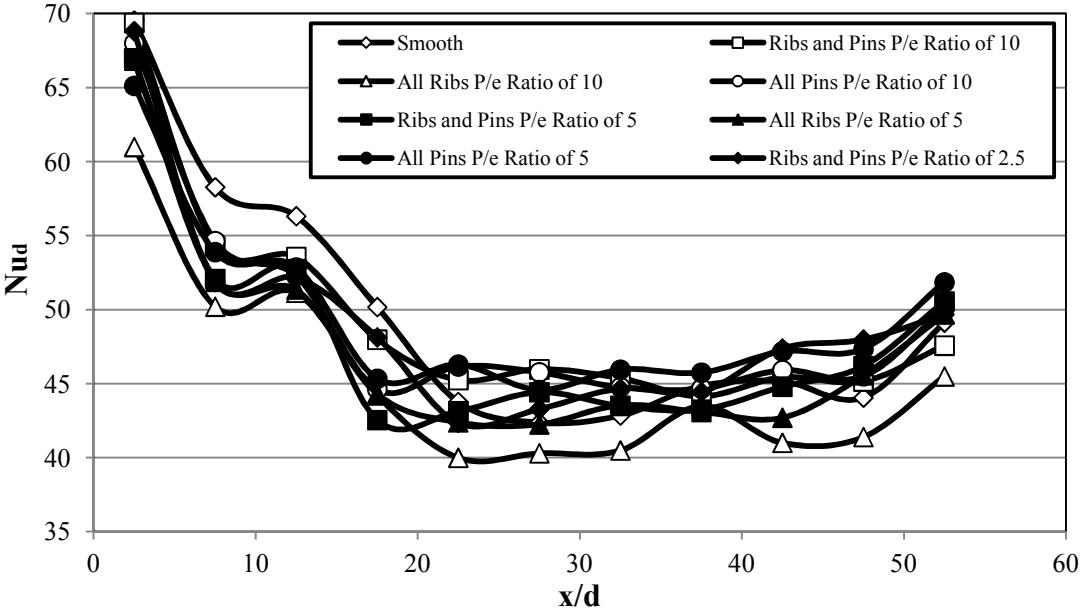

Figure 52 - Nusselt number comparison for jet impingement at Re=20K.

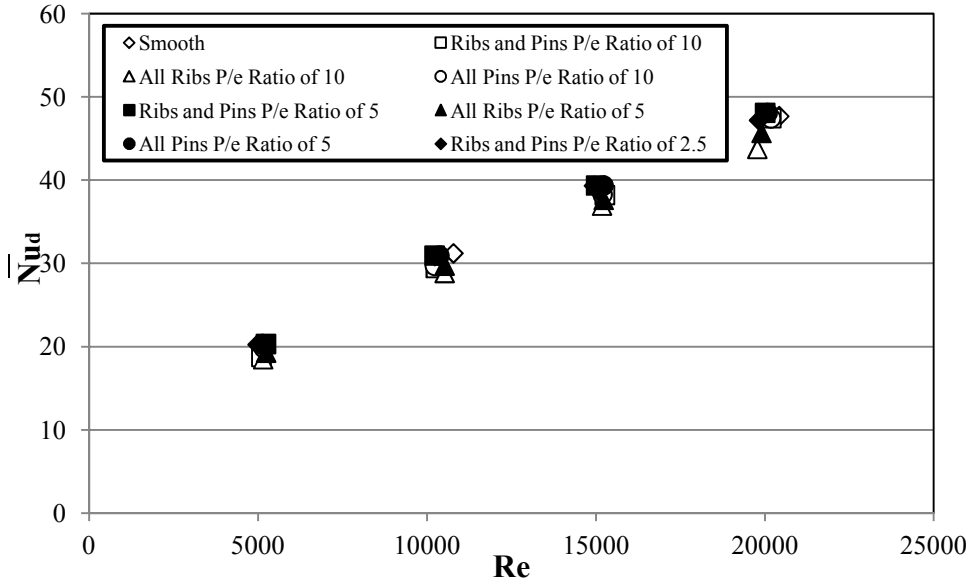

Figure 53 – Average Nusselt number for jet impingement cases.

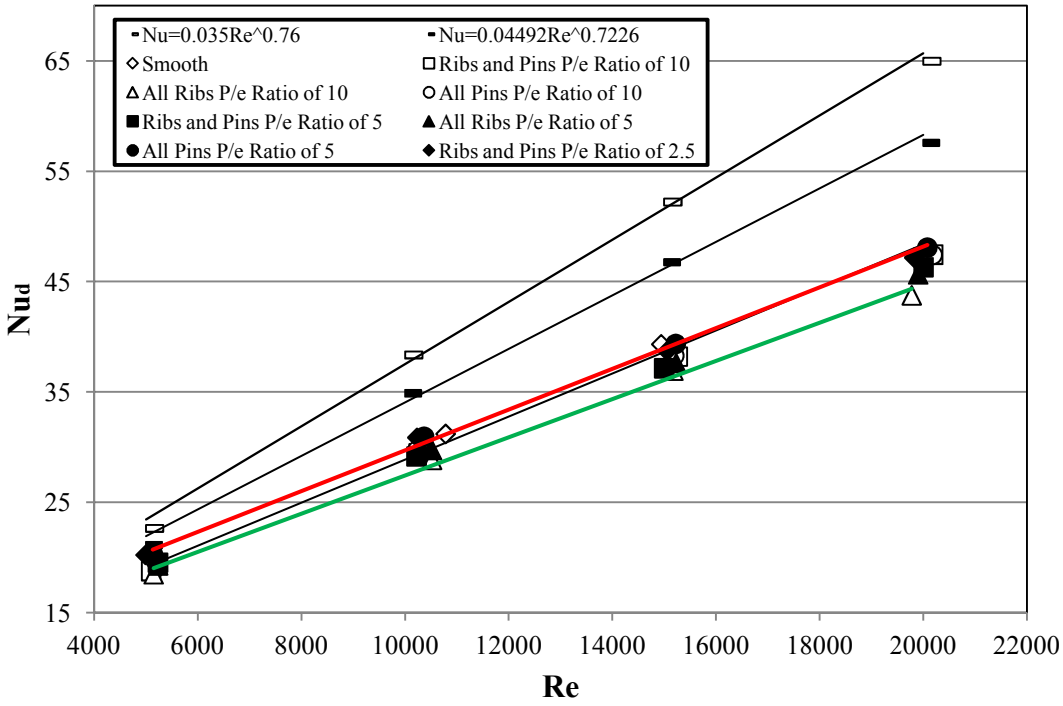

Figure 54 – Empirical Nusselt number ratio for jet impingement.

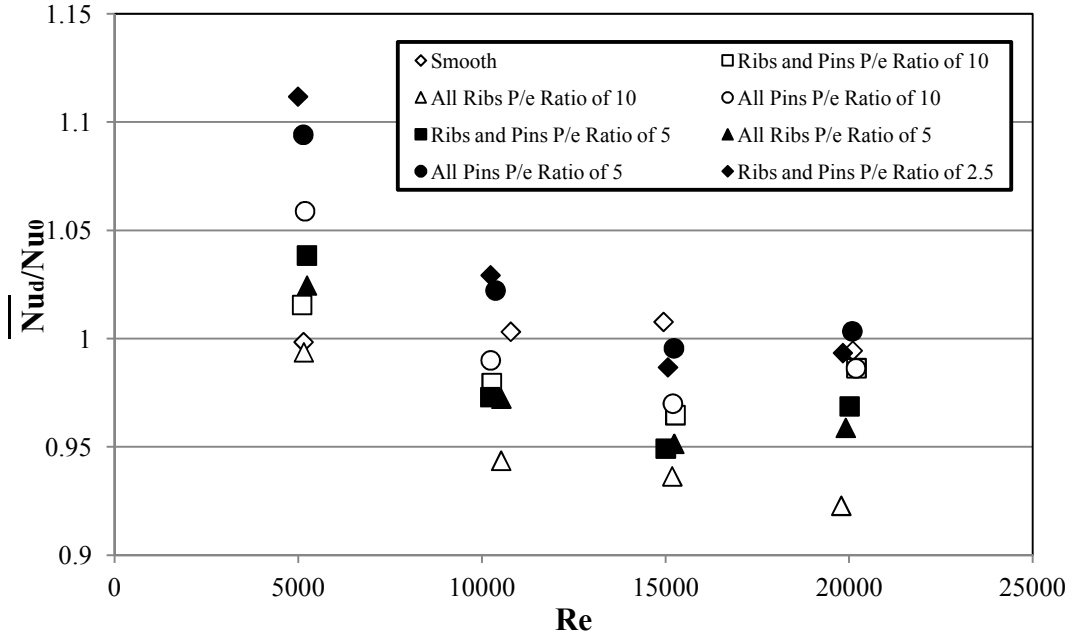

Figure 55 –Average Nusselt number ratio for jet impingement cases.

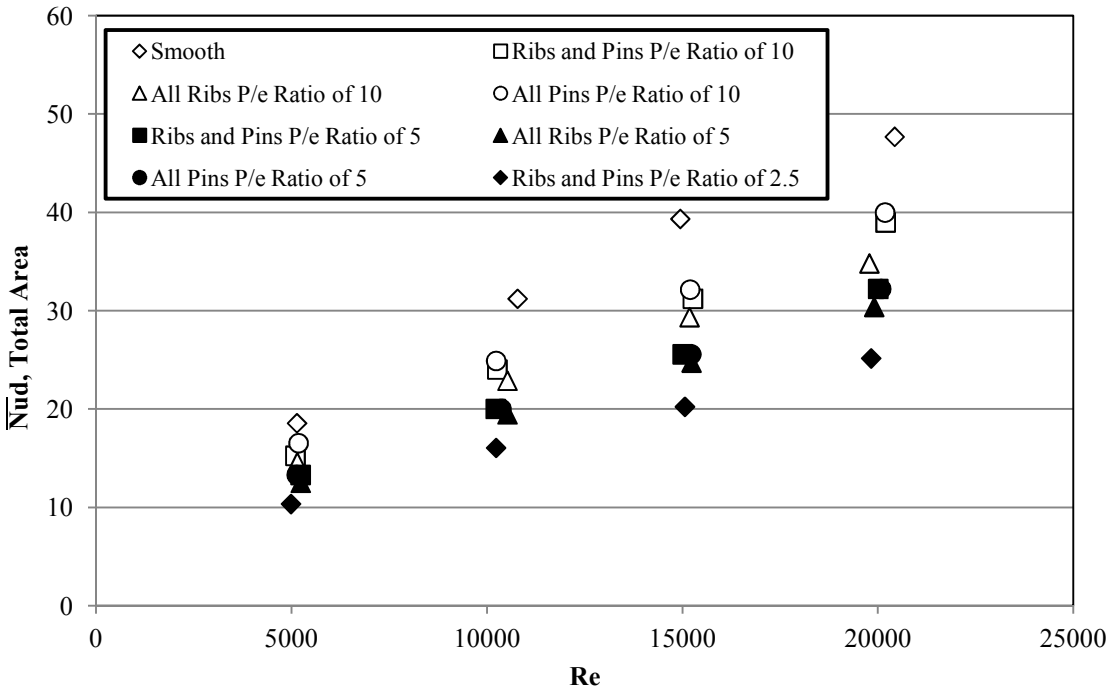

Figure 56 – Average Nusselt number based on total area for jet impingement cases.

Table 8 - Cross-flow percentage for smooth case.

	Cross Flow %			
Region	Re=5K	Re=10K	Re=15K	Re=20K
1	3.93%	3.93%	3.93%	3.93%
2	7.88%	7.89%	7.89%	7.88%
3	11.68%	11.70%	11.70%	11.69%
4	15.43%	15.47%	15.46%	15.45%
5	19.42%	19.46%	19.44%	19.40%
6	22.71%	22.81%	22.78%	22.78%
7	26.75%	26.91%	26.91%	26.91%
8	29.82%	29.97%	29.92%	29.92%
9	33.35%	33.54%	33.48%	33.48%
10	36.85%	37.08%	37.00%	37.01%
11	40.31%	40.58%	40.49%	40.50%
12	43.17%	43.47%	43.35%	43.38%
	Cd			
	0.8906	0.8518	0.83631	0.83114

Table 9 - Cross-flow percentage for all ribs P/e ratio of 10 case.

	Cross Flow %			
Region	Re=5K	Re=10K	Re=15K	Re=20K
1	3.93%	3.93%	3.93%	3.93%
2	7.88%	7.90%	7.90%	7.89%
3	11.65%	11.67%	11.67%	11.66%
4	15.35%	15.38%	15.38%	15.37%
5	19.30%	19.38%	19.40%	19.39%
6	22.49%	22.53%	22.53%	22.52%
7	26.63%	26.71%	26.69%	26.60%
8	29.41%	29.46%	29.48%	29.49%
9	32.85%	32.92%	32.94%	32.95%
10	36.26%	36.34%	36.37%	36.37%
11	39.63%	39.72%	39.76%	39.77%
12	42.29%	42.32%	42.39%	42.45%
	Cd			
	0.91496	0.861817	0.848937	0.86192

Table 10 - Cross-flow percentage for all ribs P/e ratio of 5 case.

	Cross Flow %			
Region	Re=5K	Re=10K	Re=15K	Re=20K
1	3.93%	3.93%	3.93%	3.93%
2	7.91%	7.89%	7.90%	7.90%
3	11.67%	11.67%	11.66%	11.67%
4	15.35%	15.37%	15.36%	15.36%
5	19.42%	19.38%	19.37%	19.36%
6	22.43%	22.52%	22.49%	22.47%
7	26.62%	26.67%	26.67%	26.72%
8	29.30%	29.46%	29.40%	29.36%
9	32.73%	32.91%	32.85%	32.80%
10	36.12%	36.33%	36.26%	36.20%
11	39.47%	39.72%	39.63%	39.56%
12	42.01%	42.35%	42.22%	42.10%
	Cd			
	0.9183	0.87452	0.86902	0.86967

Table 11 - Cross-flow percentage for all pins P/e ratio of 5 case.

	Cross Flow %			
Region	Re=5K	Re=10K	Re=15K	Re=20K
1	3.93%	3.93%	3.93%	3.93%
2	7.89%	7.90%	7.89%	7.89%
3	11.65%	11.67%	11.67%	11.67%
4	15.35%	15.39%	15.40%	15.40%
5	19.32%	19.39%	19.40%	19.40%
6	22.48%	22.55%	22.61%	22.60%
7	26.59%	26.72%	26.69%	26.69%
8	29.39%	29.51%	29.63%	29.61%
9	32.84%	32.98%	33.12%	33.10%
10	36.24%	36.41%	36.58%	36.55%
11	39.61%	39.81%	40.00%	39.97%
12	42.28%	42.45%	42.75%	42.71%
	Cd			
	0.89798	0.849774	0.843198	0.845996

Table 12 - Cross-flow percentage for all pins P/e ratio of 10 case.

	Cross Flow %			
Region	Re=5K	Re=10K	Re=15K	Re=20K
1	3.93%	3.93%	3.93%	3.93%
2	7.89%	7.89%	7.88%	7.89%
3	11.68%	11.69%	11.68%	11.69%
4	15.42%	15.44%	15.42%	15.44%
5	19.44%	19.44%	19.38%	19.46%
6	22.66%	22.73%	22.68%	22.71%
7	26.75%	26.83%	26.80%	26.80%
8	29.71%	29.84%	29.73%	29.82%
9	33.23%	33.38%	33.25%	33.35%
10	36.70%	36.88%	36.73%	36.85%
11	40.14%	40.35%	40.18%	40.32%
12	42.95%	43.19%	42.96%	43.14%
	Cd			
	0.90755	0.86837	0.8547	0.82558

Table 13 - Cross-flow percentage for ribs and pins P/e ratio of 10 case.

	Cross Flow %			
Region	Re=5K	Re=10K	Re=15K	Re=20K
1	3.93%	3.93%	3.93%	3.93%
2	7.88%	7.88%	7.88%	7.89%
3	11.68%	11.69%	11.69%	11.68%
4	15.43%	15.45%	15.45%	15.42%
5	19.40%	19.47%	19.48%	19.50%
6	22.71%	22.75%	22.75%	22.65%
7	26.75%	26.78%	26.76%	26.57%
8	29.81%	29.90%	29.90%	29.74%
9	33.34%	33.45%	33.46%	33.26%
10	36.83%	36.97%	36.98%	36.74%
11	40.29%	40.45%	40.46%	40.19%
12	43.16%	43.34%	43.37%	43.06%
	Cd			
	0.906181	0.869517	0.854532	0.850584

Table 14 - Cross-flow percentage for ribs and pins P/e ratio of 5 case.

	Cross Flow %			
Region	Re=5K	Re=10K	Re=15K	Re=20K
1	3.93%	3.93%	3.93%	3.93%
2	7.89%	7.89%	8.02%	7.90%
3	11.65%	11.66%	11.93%	11.66%
4	15.34%	15.36%	15.83%	15.35%
5	19.33%	19.38%	18.90%	19.40%
6	22.44%	22.50%	21.98%	22.44%
7	26.59%	26.60%	26.09%	26.59%
8	29.32%	29.44%	28.93%	29.32%
9	32.75%	32.89%	32.39%	32.75%
10	36.14%	36.30%	35.82%	36.14%
11	39.49%	39.68%	39.20%	39.50%
12	42.11%	42.33%	41.83%	42.05%
	Cd			
	0.918911	0.871354	0.861964	0.860841

Table 15 - Cross-flow percentage for ribs and pins P/e Ratio of 2.5 case.

	Cross Flow %			
Region	Re=5K	Re=10K	Re=15K	Re=20K
1	3.93%	3.93%	3.93%	3.93%
2	7.91%	7.90%	7.90%	7.91%
3	11.64%	11.65%	11.64%	11.64%
4	15.30%	15.33%	15.31%	15.29%
5	19.36%	19.35%	19.34%	19.32%
6	22.30%	22.39%	22.33%	22.26%
7	26.50%	26.56%	26.51%	26.49%
8	29.07%	29.22%	29.14%	29.01%
9	32.45%	32.63%	32.53%	32.37%
10	35.79%	36.00%	35.88%	35.70%
11	39.09%	39.33%	39.20%	38.99%
12	41.54%	41.85%	41.68%	41.40%
	Cd			
	0.912434	0.868712	0.85824	0.862415

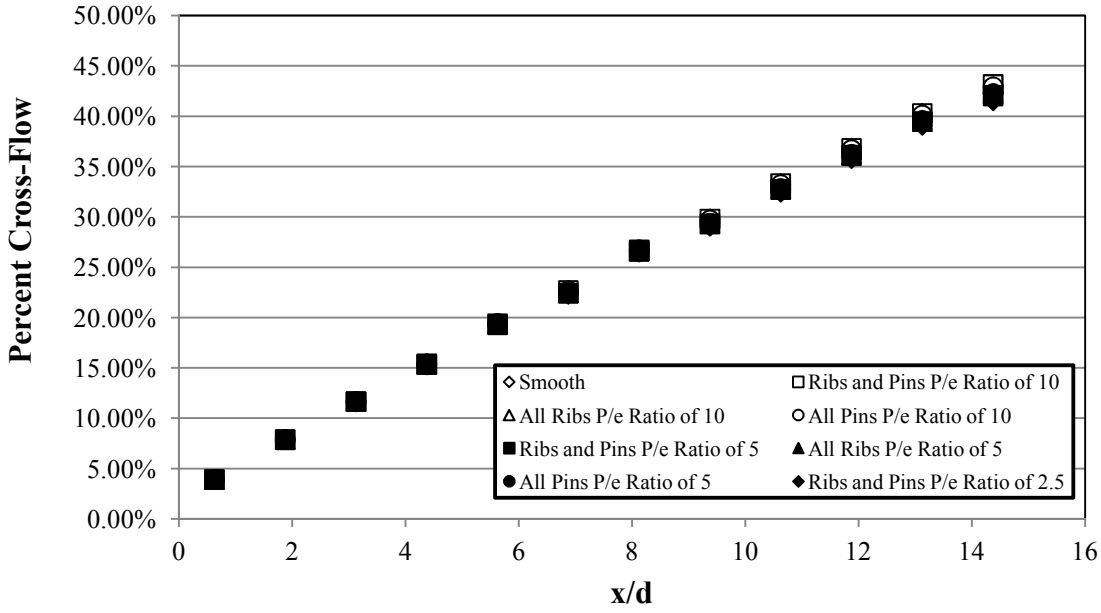

Figure 57 – Cross-flow results for Re=5K.

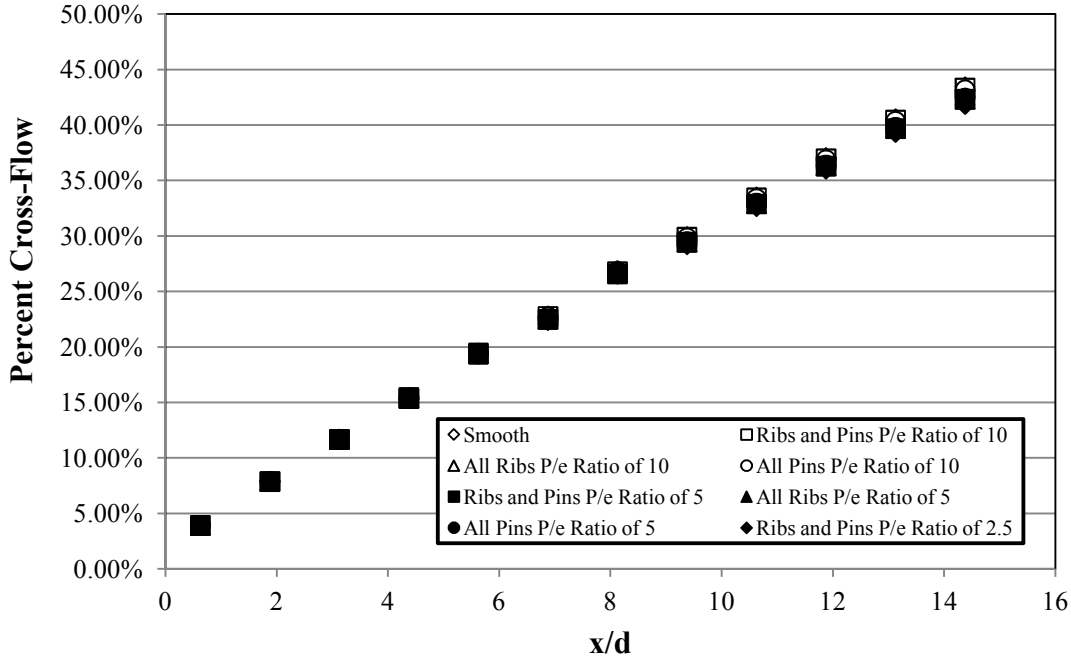

Figure 58 – Cross-flow results for Re=10K.

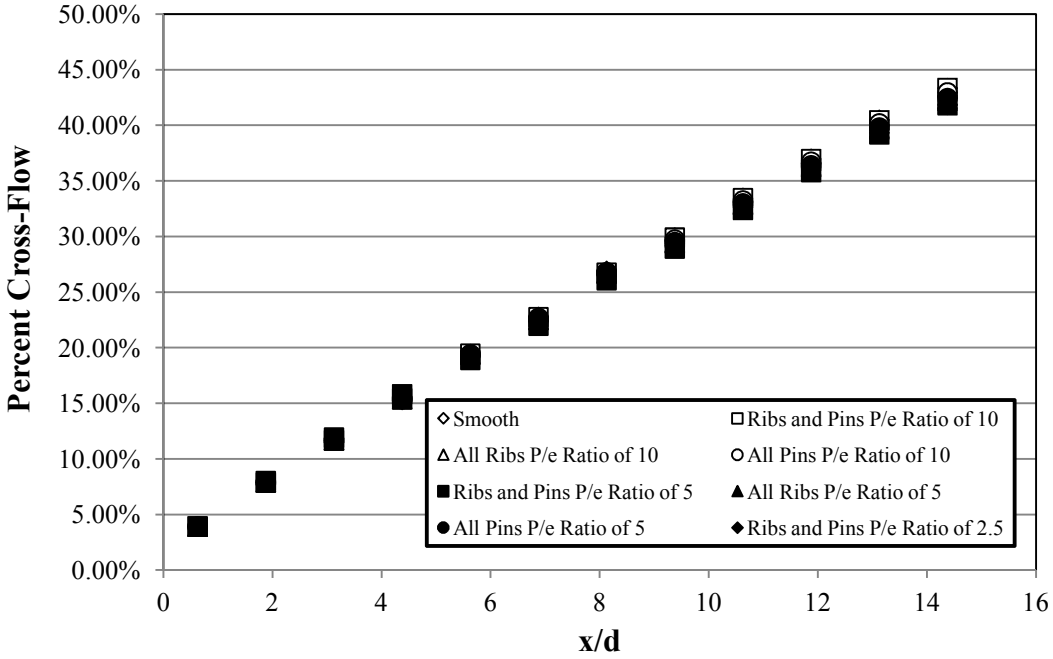

Figure 59 – Cross-flow results for Re=15K.

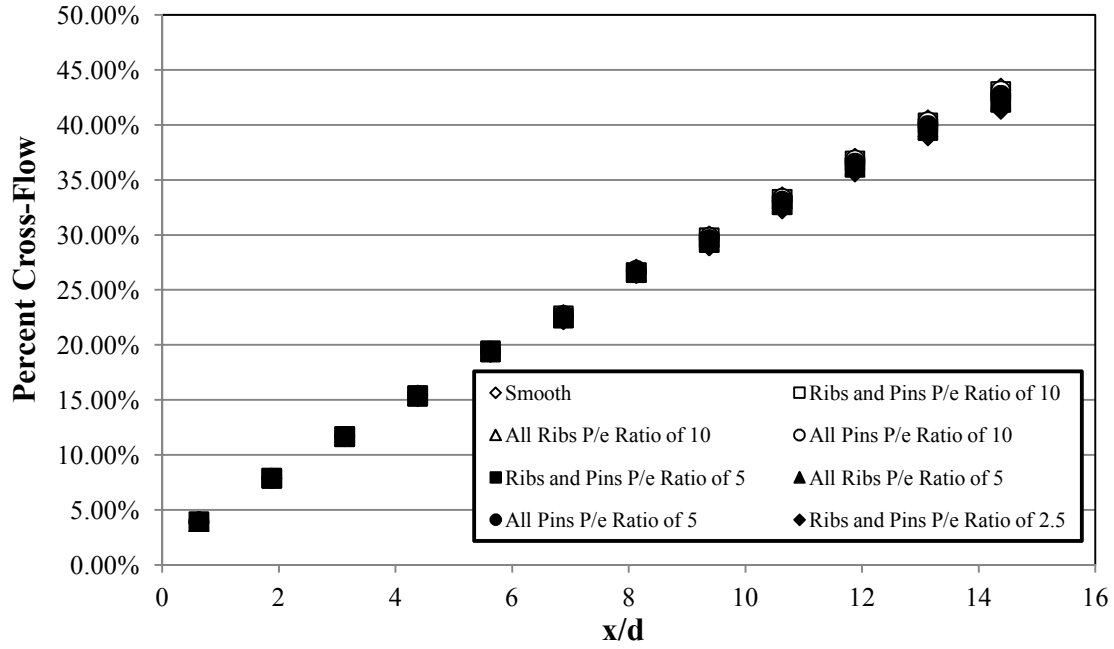

Figure 60 – Cross-Flow Results for Re=20K.

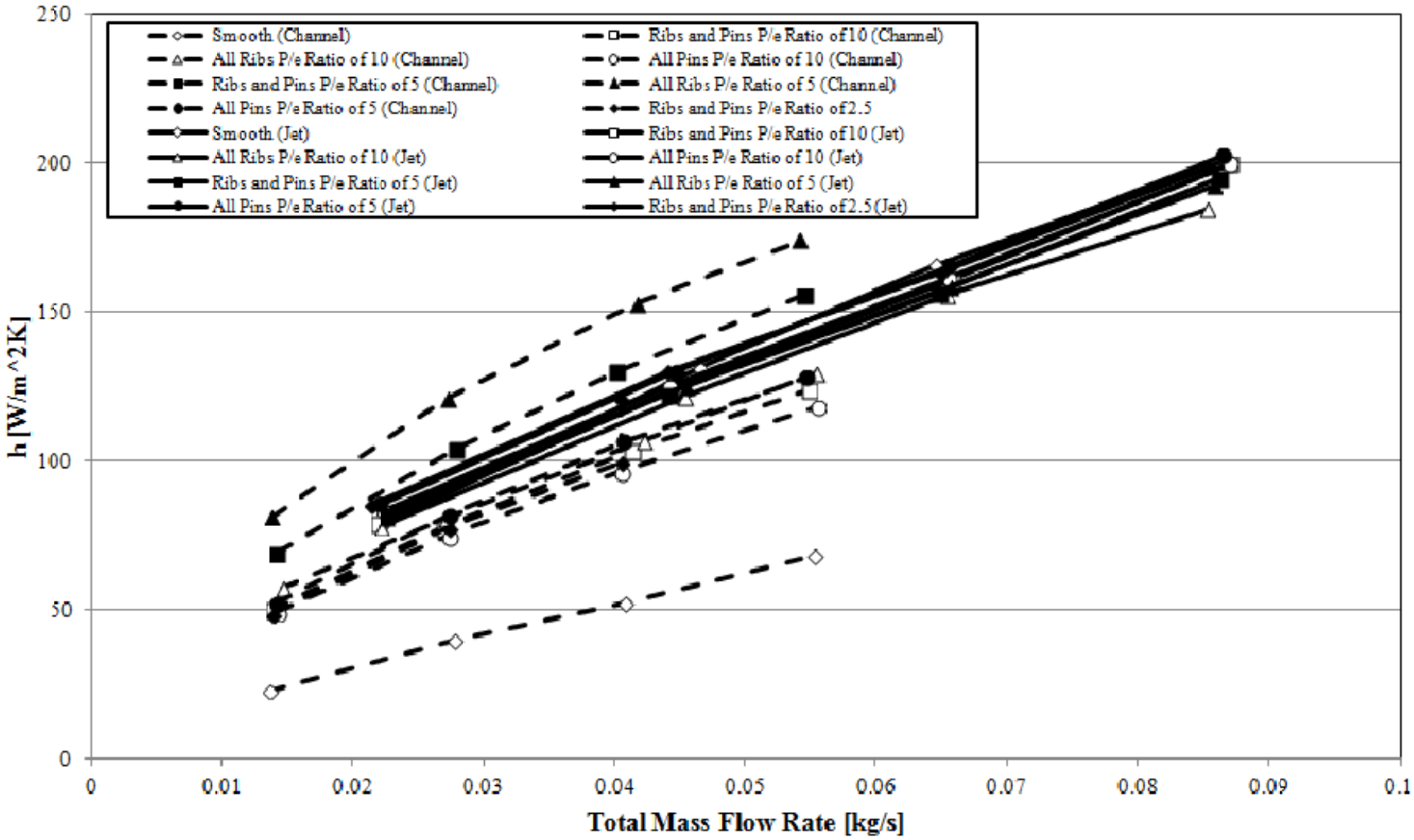

Figure 61 – Heat transfer coefficient for all of the cases.

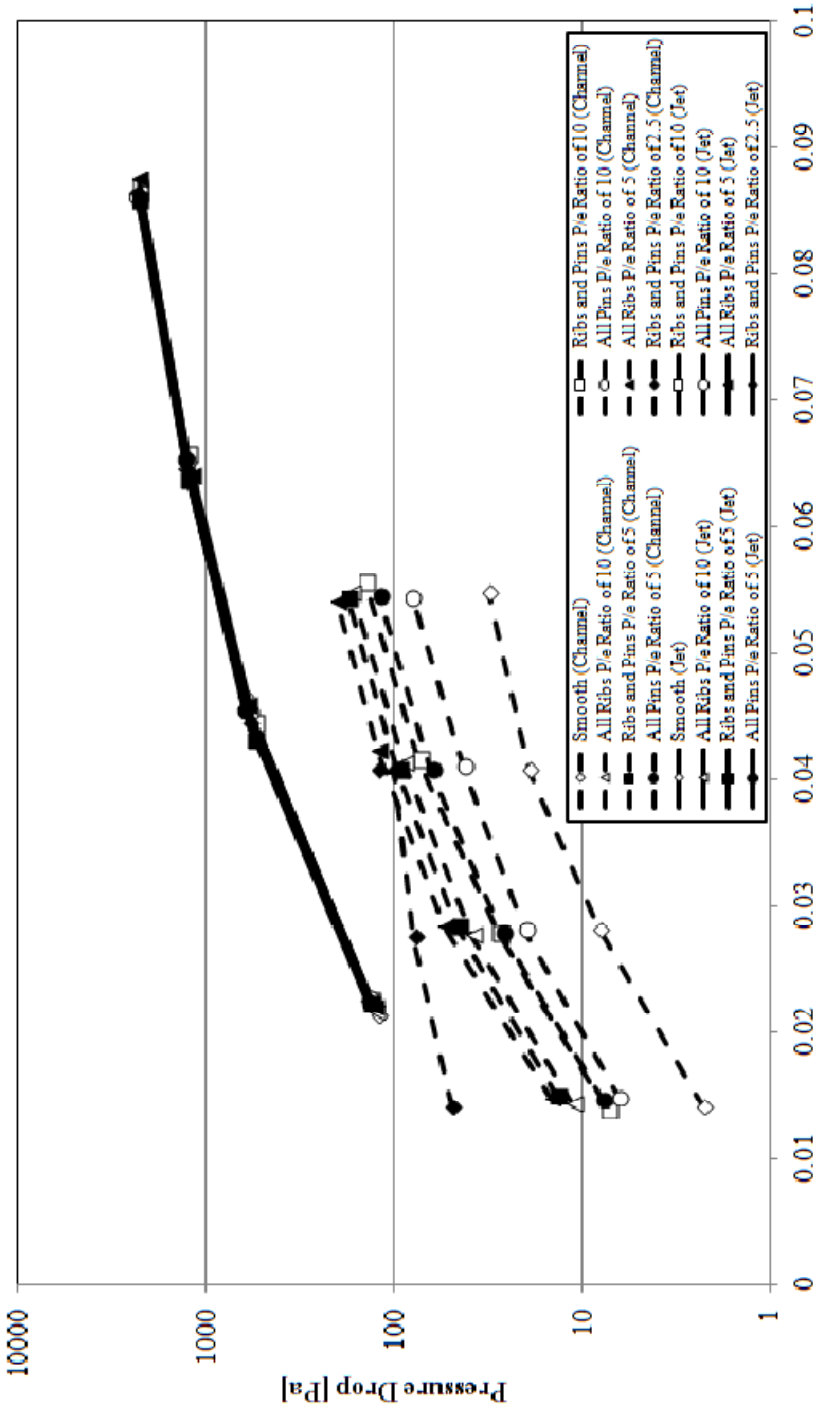

Figure 62 – Pressure Drop for All of the Cases

CALCULAION OF FLOW COEFFICIENT

(Provided from Fu [18] p.3-5, 10-11)

Flow Coefficient, K:

$$K \equiv \frac{C_d}{\sqrt{1-\beta^4}} \tag{21}$$

where β is the diameter ratio,

$$\beta = \frac{D_2}{D_1} \tag{22}$$

The Flow Coefficient depends on the measurement of pressure drop across the orifice. It is a function of Reynolds number, diameter ratio and diameters of the pipe and throat. ASME has provided several types of pressure drop measurement. Since the pressure drop may be very small, a little difference will result in a large error in the calculation of flow rate. Iteration is needed to obtain flow coefficient.

For Flange Taps:

$$K = K_0(1+\frac{\beta A}{\mathrm{Re}_{D_1}}) \tag{23}$$

$$K_0 = K_e(\frac{10^6 D_2}{10^6 D_2 + 15A}) \tag{24}$$

$$K_e = 0.5993 + \frac{0.007}{D_1} + (0.364 + \frac{0.076}{\sqrt{D_1}})\beta^4 + 0.4(1.6 - \frac{1}{D_1})^5 \left[(0.07 + \frac{0.5}{D_1}) - \beta \right]^{5/2} - (0.009 + \frac{0.034}{D_1})(0.5 - \beta)^{3/2} + (\frac{65}{D_1^{\,2}} + 3)(\beta - 0.7)^{5/2} \quad (25)$$

$$A = D_2(830 - 5000\beta + 9000\beta^2 - 4200\beta^3 + \frac{530}{D_1}) \quad (26)$$

(The coefficient for the fourth term in equation (KF-4) should be 4200. At ASME report, it was 42000.)

For a 2.0 in diameter pipe and 1.0 in diameter orifice, the last three terms in K_e will include negative value with fractional exponents or zero. In this case, according to Reference 3, they will be assumed zero. However, the value of Flow Coefficient will be different from ASME Table. The suggestion is that take the absolute value for the fourth term and multiply it times ½. The last two terms can be assumed as zero. The differences of changing the fourth term are compared on Table 2. From Table 2, including half the value of the fourth term can obtain a value more close to ASME's data. For Reynolds number higher than 15000, the fourth term can be neglected. The Reynolds number here is based on pipe diameter. Therefore, the equation (KF-3) will become

$$K_e = 0.5993 + \frac{0.007}{D_1} + (0.364 + \frac{0.076}{\sqrt{D_1}})\beta^4 + 0.4(1.6 - \frac{1}{D_1})^5 \left[\beta - (0.07 + \frac{0.5}{D_1}) \right]^{5/2} \times \frac{1}{2} \quad (27)$$

or

$$K_e = 0.5993 + \frac{0.007}{D_1} + (0.364 + \frac{0.076}{\sqrt{D_1}})\beta^4 \quad (28)$$

Using D_1=2.0 in, D_2=1.0 in, β=0.5, these parameters can be specified as

$Re_{D1} \leq 15000$: A=320, K_e=0.6333364, K_0=0.6303109

$$K = 0.6303109 \times (1 + \frac{160}{R_{D_1}}) \quad (29)$$

$Re_{D1} \geq 15000$: A=320, K_e=0.6289088, K_0=0.6259045

$$K = 0.6259045 \times (1 + \frac{160}{R_{D_1}}) \quad (30)$$

Calculate mass flow rate using an initial guessing value (0.63) for flow coefficient K, using Eq. (1). Iteration is needed in obtaining K value. Normally, flow coefficient K is in the range from 0.62 to 0.65. Based on the calculated mass flow rate, obtain the Reynolds number at the pipe. Calculate the new flow coefficient K (Equation (30)), using the new Reynolds number. Repeat these steps using the new K-value. After several times iterations, the mass flow rate and K-value can be determined under given conditions. Compare the mass flow rate to the required mass flow rate which is obtained at Step 1. Make further adjustment if needed.